

## Exploring cosmological gravitational wave backgrounds through the synergy of LISA and the Einstein Telescope

Alisha Marriott-Best<sup>1,\*</sup>, Debika Chowdhury<sup>2,†</sup>, Anish Ghoshal<sup>3,‡</sup> and Gianmassimo Tasinato<sup>1,4,§</sup>

<sup>1</sup>*Physics Department, Swansea University, Wales SA2 8PP, United Kingdom*

<sup>2</sup>*Indian Institute of Astrophysics, II Block, Koramangala, Bengaluru 560034, India*

<sup>3</sup>*Institute of Theoretical Physics, Faculty of Physics, ul. Pasteura 5, 02-093 Warsaw, Poland*

<sup>4</sup>*Dipartimento di Fisica e Astronomia, Università di Bologna, INFN, Sezione di Bologna, I.S. FLAG, viale B. Pichat 6/2, 40127 Bologna, Italy*



(Received 14 September 2024; accepted 21 March 2025; published 1 May 2025)

The gravitational wave (GW) interferometers Laser Interferometer Space Antenna (LISA) and the Einstein Telescope (ET) are expected to be functional in the next decade(s), possibly around the same time. They will operate over different frequency ranges, with similar integrated sensitivities to the amplitude of a stochastic GW background (SGWB). We investigate the synergies between these two detectors, in terms of a multiband detection of a cosmological SGWB characterized by a large amplitude, and a broad frequency spectrum. We develop the notion of integrated sensitivity and propose a novel signal-to-noise ratio optimal for characterization of the geometrical properties of the interferometer systems of LISA and the ET operating simultaneously. By investigating various examples of SGWBs, such as those arising from cosmological phase transition, cosmic string, and primordial inflation, we show that LISA and the ET operating together will have the opportunity to assess more effectively the characteristics of the GW spectrum produced by the same cosmological source, but at separate frequency scales. Moreover, the two experiments in tandem can be sensitive to features of early Universe cosmic expansion before big bang nucleosynthesis (BBN), which affects the SGWB frequency profile and which would not be possible to detect otherwise, since two different frequency ranges correspond to two different pre-BBN (or postinflationary) epochs. Besides considering the GW spectrum, we additionally undertake a preliminary study of the sensitivity of LISA and the ET to soft limits of higher-order tensor correlation functions. Given that these experiments operate at different frequency bands, their synergy constitutes an ideal direct probe of squeezed limits of higher-order GW correlators, which cannot be measured operating with a single instrument only.

DOI: [10.1103/PhysRevD.111.103001](https://doi.org/10.1103/PhysRevD.111.103001)

### I. INTRODUCTION

The detection of gravitational waves (GWs) from astrophysical sources by the LIGO-Virgo Collaboration in 2015 [1] opened up a new window into GW astronomy. For cosmology, upcoming upgrades of LIGO-Virgo [2] and proposed future detectors such as Laser Interferometer Space Antenna (LISA) [3], BBO-DECIGO [4], the Einstein Telescope (ET) [5,6], and Cosmic Explorer [7] will also open up a new possible observational window into the early Universe. Unlike photons, the gravitons (primordial GWs) that were produced in the early Universe can propagate freely throughout cosmic history and therefore would constitute ideal messengers of the history of the Universe [8–10].

In fact, the recent hints of detection of a stochastic gravitational wave background (SGWB) in the nHz regime by Pulsar Timing Array Collaborations [11–14] initiated the era of experimental characterization of the SGWB. Still, much has to be done to distinguish between different sources of SGWB, astrophysical or cosmological (see, e.g., Refs. [15,16] for recent topical reviews on SGWB sources and detection techniques).

The next generation of GW detectors promises to improve upon the current experimental sensitivity to SGWB in frequency ranges between mHz and decahertz, much higher than the nHz regime probed by pulsar timing arrays. These higher-frequency regimes are more suitable for detecting GWs produced by various early Universe cosmic sources, such as those arising from phase transitions, cosmic strings, cosmological inflation, etc. Early Universe scenarios can lead to a SGWB with intriguing properties such as a rich frequency profile, chirality, and non-Gaussianity, all of which are important to accurately characterise for future targets (see, e.g., Ref. [17] for a

\*Contact author: [2347066@swansea.ac.uk](mailto:2347066@swansea.ac.uk)

†Contact author: [debika.chowdhury@iiap.res.in](mailto:debika.chowdhury@iiap.res.in)

‡Contact author: [anish.ghoshal@fuw.edu.pl](mailto:anish.ghoshal@fuw.edu.pl)

§Contact author: [g.tasinato2208@gmail.com](mailto:g.tasinato2208@gmail.com)

comprehensive recent review). It is essential to develop tools to detect and better characterise the SGWB in a frequency range which can be tested with high sensitivity by future experiments, say, between  $10^{-5} \leq f/\text{Hz} \leq 10^2$ . In this work, we explore such a possibility of studying the early-Universe sources of SGWB spanning this frequency range by exploiting synergies between LISA [17–19] and the ET [5,6,20,21] experiments, for a multiband detection of the SGWB. Both experiments are planned to take data in the next decade and will have similar sensitivities to the amplitude of SGWB. Hence it is interesting to inquire what we can gain from detecting a SGWB with both the experimental facilities.

While LISA will have its maximal sensitivity for frequencies  $f$  in the mHz regime, the ET will be more sensitive to signals in the decahertz range. If the SGWB has a broad enough frequency profile and a sufficiently large amplitude, it will be advantageous to have both the experiments detecting its features in different frequency ranges. We can then measure the properties of the GW source more accurately and study aspects of early-Universe cosmology which cannot be probed by each single experiment.

In the context of beyond the Standard Model (BSM) of particle physics, there are several concrete predictions of SGWBs over multiband frequency ranges as we will discuss below. First, the very-well-understood temperature anisotropies in the cosmic microwave background (CMB) radiation superimposed on the perfectly smooth background implies that the Universe at the very beginning has undergone an accelerated expansion, a phenomenon also known as the cosmic inflation [22–25]. However, the history of the primordial universe postinflation (plausibly after temperature  $T \leq 10^{14}$  GeV) and before the beginning of big bang nucleosynthesis (BBN), that is the at temperature above the Standard Model (SM) plasma temperature of  $T \gtrsim 1$  MeV, remains unconstrained by any observational data at the moment. The standard assumption that the pre-BBN universe is filled with radiation and becomes radiation dominated after the end of the inflationary phase is often challenged by open problems in the SM of particle physics, e.g., the microscopic origin of dark matter (DM), the explanation for the observed matter-antimatter asymmetry, the flavor puzzle, or the ultraviolet SM Higgs field dynamics, the strong  $CP$  problem (see, e.g., Refs. [26,27] for a review). Introducing new BSM physics which resolves these puzzles of modern particle physics and cosmology often is associated with new energy scales (other than the electroweak or Planck scales) and on many occasions new degrees of freedom (like new particles) or interactions which sometimes generate deviations from the standard radiation domination era before the onset of BBN.

We start our work with Sec. II explaining why and how a detection of the SGWB in synergy between LISA and the ET can improve the signal-to-noise ratio (SNR) on the

measurements of parameters characterizing a SGWB with a broad frequency spectrum. We then move on to Sec. III to discuss and analyze several early-Universe scenarios that are able to produce GWs spanning over a broad frequency range. By means of a Fisher analysis, we quantitatively demonstrate how a detection of GW with the two experiments together can help us to measure specific model parameters. Section IV discusses the notion of integrated sensitivity curves, which offer a simple visual aid to demonstrate the advantages of the synergy between the two experiments with regard to detecting SGWB with certain frequency shapes. Cosmological SGWB can be characterized by non-Gaussian features, which motivate the study of  $n$ -point correlation functions going beyond the GW power spectrum and energy density. Given that LISA and ET operate in different frequency ranges which corresponding to different energy scales of tensor Fourier modes, in Sec. V, we address the problem of the detectability of soft limits of  $n$ -point correlation functions, discussing the response function of the LISA-ET system to such observables. We conclude in Sec. VI. A technical Appendix complements our arguments. We work with natural units  $c = \hbar = 1$ . We fix the  $h$  in the Hubble parameter as  $h = 0.67$ .

## II. SYNERGIES BETWEEN LISA AND THE EINSTEIN TELESCOPE

The aim of this section is to start discussing in practical terms the possibility of making a synergetic detection of a SGWB with the LISA and ET instruments. In the next section, we will describe theoretical motivations to do so.

### A. Gravitational waves and their detection

GWs are associated with spin-2 fluctuations  $h_{ij}$  of the Minkowski metric:

$$ds^2 = -dt^2 + (\delta_{ij} + h_{ij}(t, \vec{x}))dx^i dx^j. \quad (2.1)$$

We decompose  $h_{ij}$  into Fourier modes as

$$h_{ij}(t, \vec{x}) = \sum_{\lambda} \int_{-\infty}^{+\infty} df \int d^2 \hat{n} e^{-2\pi i f \hat{n} \cdot \vec{x}} e^{2\pi i f t} \mathbf{e}_{ij}^{\lambda}(\hat{n}) h_{\lambda}(f, \hat{n}), \quad (2.2)$$

imposing the condition

$$h_{\lambda}(-f, \hat{n}) = h_{\lambda}^*(f, \hat{n}), \quad (2.3)$$

which ensures that  $h_{ij}(t, \vec{x})$  is a real function. The quantities  $f$ ,  $\hat{n}$ , and  $\lambda$  denote, respectively, the GW frequency, direction, and polarization ( $\lambda = +, \times$ ). In the previous expressions, we have decomposed the GW momentum as  $\vec{k} = 2\pi f \hat{n}$ , with  $f$  being the GW frequency and  $\hat{n}$  being

its direction. We assume that the polarization tensors  $\mathbf{e}_{ij}^\lambda$  are real quantities. We adopt a  $(+, \times)$  basis and use the normalization  $\sum_{ij} \mathbf{e}_{ij}^\lambda \mathbf{e}_{ij}^{\lambda'} = 2\delta^{\lambda\lambda'}$ .

We assume in this section that the SGWB is isotropic, stationary, and Gaussian. The GW energy density is expressed in terms of the function  $\Omega_{\text{GW}}(f)$ , defined starting from the two-point function for GW Fourier modes (see, e.g., Ref. [28]). It is defined as

$$\Omega_{\text{GW}}(f) = \left( \frac{4\pi^2}{3H_0^2} \right) f^3 I(f), \quad (2.4)$$

where the GW intensity  $I(f)$  is given by

$$\langle (h^\lambda(f, \hat{n}))^* h^{\lambda'}(f', \hat{n}') \rangle = \frac{\delta^{\lambda\lambda'} \delta(\hat{n} - \hat{n}')}{2} \frac{\delta(f - f')}{4\pi} I(f). \quad (2.5)$$

We shall now discuss how the interferometers LISA and ET respond to the presence of GWs. Their behavior depends on the so-called response functions and on the sources of noise which affect a possible GW detection. For the case of LISA, this topic is explained in a clear and pedagogical way in Ref. [29], which we briefly review here (see also Ref. [30] for a more systematic discussion). We extend their analysis to include ET<sup>1</sup> and the synergy between the two detectors. We mainly use the notation and conventions of Ref. [29], adapting them to the present context.

We assume that both the LISA and the ET instruments have shapes corresponding to equilateral triangles.<sup>2</sup> The GW is detected as an effect of the time difference between signals measured at different vertices of the triangular interferometer. We shall denote the three vertices of a triangle (it can be the LISA or the ET instrument) with the combination of letters  $(abc)$ . Let us consider the vertex  $a$  as a reference. The instrument measures the phase difference  $\Phi$ ,

$$\Phi_{abc} = \Delta\varphi_{abc} + n_{abc} \quad (2.6)$$

of the GW signals traveling along the arms  $(ab)$  and  $(ac)$ , plus the contribution  $n$  of noise. In what follows, we will neglect the time dependence of the positions of the detectors.

The interferometer response and the GW signal contribution can then be expanded in Fourier modes as

$$\Delta\varphi_{abc}(t) = \int_{-\infty}^{+\infty} df e^{2\pi i f t} \Delta\tilde{\varphi}_{abc}(f), \quad (2.7)$$

where the signal Fourier mode  $\Delta\tilde{\varphi}$  is given by the combination of the spin-2 mode  $h^\lambda(f, \hat{n})$  and the interferometer

response  $F_{abc}^\lambda$ , as contained in the following definition:

$$\Delta\tilde{\varphi}_{abc}(f) = \sum_{\lambda} \int d^2n h^\lambda(f, \hat{n}) F_{abc}^\lambda(f, \hat{n}). \quad (2.8)$$

The quantity  $F_{abc}^\lambda$  is expressed as

$$F_{abc}^\lambda(f, \hat{n}) = \frac{e^{-2\pi i f \hat{n} \cdot \vec{x}_a}}{2} \mathbf{e}_{ij}^\lambda(\hat{n}) \left[ \mathcal{F}^{ij}(\hat{\ell}_{ab} \cdot \hat{n}, f) - \mathcal{F}^{ij}(\hat{\ell}_{ac} \cdot \hat{n}, f) \right], \quad (2.9)$$

with the unit vector  $\hat{\ell}$  corresponding to the direction of the detector arm. The geometry of the detector enters into the functions  $\mathcal{F}^{ij}$ . Their expressions depend on the type of interferometer one considers—space based (LISA) or ground based (ET). For the case of LISA, they read

$$\begin{aligned} \mathcal{F}_{\text{LISA}}^{ij}(\hat{\ell} \cdot \hat{n}, f) &= \frac{\hat{\ell}^i \hat{\ell}^j}{2} e^{-i f (3 + \hat{\ell} \cdot \hat{n}) / (2f_\star)} \text{sinc}\left(\frac{f}{2f_\star} (1 - \hat{\ell} \cdot \hat{n})\right) \\ &\quad + \frac{\hat{\ell}^i \hat{\ell}^j}{2} e^{-i f (1 + \hat{\ell} \cdot \hat{n}) / (2f_\star)} \text{sinc}\left(\frac{f}{2f_\star} (1 + \hat{\ell} \cdot \hat{n})\right), \end{aligned} \quad (2.10)$$

where the pivot scale  $f_\star = 1/(2\pi L)$ —with  $L$  being the length of the interferometer arms—is of the order of the mHz frequencies probed by LISA. In contrast, the expression for  $\mathcal{F}$  is much simpler for a ground-based detector such as the ET and corresponds to the following low-frequency limit of the previous equation:

$$\mathcal{F}_{\text{ET}}^{ij}(\hat{\ell} \cdot \hat{n}, f) = \hat{\ell}^i \hat{\ell}^j. \quad (2.11)$$

Starting from the above formulas, we can measure the phase difference of signals traveling between the arms  $(ab)$  and  $(ac)$  and correlate signals measured at different vertices by computing their two-point functions. They depend on the GW intensity  $I(f)$  [see Eq. (2.5)], weighted by the instrument response to the GW signal, and on possible noise sources. The signal two-point function in Fourier space reads

$$\begin{aligned} \langle \Phi_{abc}(f) \Phi_{xyz}(f') \rangle &= \frac{\delta(f - f')}{2} [R_{abc,xyz}(f) I(f) + N_{abc,xyz}(f)], \end{aligned} \quad (2.12)$$

with  $N_{abc,xyz}$  being the correlated noise. The signal response functions are

$$\begin{aligned} R_{abc,xyz}(f) &= \int \frac{d^2\hat{n}}{4\pi} \left[ F_{abc}^+(f, \hat{n}) F_{xyz}^+(-f, \hat{n}) \right. \\ &\quad \left. + F_{abc}^\times(f, \hat{n}) F_{xyz}^\times(-f, \hat{n}) \right]. \end{aligned} \quad (2.13)$$

<sup>1</sup>For the case of ET, the arguments leading to the definition of sensitivity curves are formally very similar, and we refer the reader, e.g., to Refs. [21,31] for transparent discussions.

<sup>2</sup>This is certain for LISA, and possible for the ET—see Ref. [32] for a discussion of various possible ET configurations.

At a given frequency  $f$ , we assume that there is neither noise correlation nor contaminations between the two detectors LISA and the ET (correlated noise is present only between arms of the same interferometer); hence, the functions  $N_{a_{bc},x_{yz}}$  are zero for correlations among vertices of two different experiments. In this section, moreover, we do not take into account correlations of the signal intensity  $I(f)$  among arms of the two different interferometers. In fact, the latter have the best sensitivities in different frequency ranges; hence, we expect that at a given frequency  $f$  the signal intensity can be at best probed by one individual experiment only. Namely, we consider only signal correlations to exist between the arms of each interferometer. Under these hypotheses, the phase covariance of the correlated signals among the different vertices of the two equilateral triangles (LISA and the ET) results in a block-diagonal  $6 \times 6$  matrix:

$$\begin{pmatrix} C_1 & C_2 & C_2 & 0 & 0 & 0 \\ C_2 & C_1 & C_2 & 0 & 0 & 0 \\ C_2 & C_2 & C_1 & 0 & 0 & 0 \\ 0 & 0 & 0 & C_3 & C_4 & C_4 \\ 0 & 0 & 0 & C_4 & C_3 & C_4 \\ 0 & 0 & 0 & C_4 & C_4 & C_3 \end{pmatrix}. \quad (2.14)$$

The upper block corresponds to the LISA, and the lower block corresponds to the ET equilateral triangle. The quantities

$$C_i = S_i + N_i$$

are combinations of (possible) GW signal ( $S_i$ ) and instrumental noise ( $N_i$ ) at each detector. This matrix can easily be diagonalized, leading to the definition of six orthogonal channels. In analogy with the names traditionally assigned to the LISA channels, these are called ( $A^\ell, E^\ell, T^\ell, A^e, E^e, T^e$ ). They are given by

$$C_{A^\ell} = C_{E^\ell} = C_1 - C_2, \quad (2.15)$$

$$C_{T^\ell} = C_1 + 2C_2, \quad (2.16)$$

$$C_{A^e} = C_{E^e} = C_3 - C_4, \quad (2.17)$$

$$C_{T^e} = C_3 + 2C_4. \quad (2.18)$$

Starting from these considerations, we can obtain the response functions for the diagonal channels, in our

approximation of static setup.<sup>3</sup> In the case of LISA, the response functions depend on the frequency; in the small-frequency limit, they can be expressed as

$$R_{A^\ell} = R_{E^\ell} = \frac{9}{20} - \frac{169}{1120} \left( \frac{f}{f_\star} \right)^2 + \mathcal{O}(f/f_\star)^4, \quad (2.20)$$

$$R_{T^\ell} = \frac{1}{4032} \left( \frac{f}{f_\star} \right)^6 + \mathcal{O}(f/f_\star)^8. \quad (2.21)$$

The complete frequency dependence of the response functions  $R_{A^\ell, E^\ell}$  and  $R_{T^\ell}$  for LISA can be easily obtained numerically, as explained in Ref. [29] (see Fig 1). Suitable analytical approximations for these two quantities are

$$R_{A^\ell, E^\ell}^{\text{fit}}(f) = \frac{9}{20} \left( 1 + \left( \frac{f}{1.25f_\star} \right)^3 \right)^{-2/3}, \quad (2.22)$$

$$R_{T^\ell}^{\text{fit}}(f) = \frac{1}{10} \left( \frac{f}{2.8f_\star} \right)^6 \left( 1 + \left( \frac{f}{2.8f_\star} \right)^6 \right)^{-4/3}, \quad (2.23)$$

which are also represented in Fig 1. The  $T$  channels  $T^\ell$  and  $T^e$  are either weakly sensitive or not sensitive at all to the GW signal (and the sensitivity in any case vanishes in the small-frequency limit). For the ground-based interferometer ET, the response functions are independent from frequency and are proportional to the zero-frequency limit of Eqs. (2.20) and (2.21): see, e.g., Ref. [31] for details.

## B. Optimal signal-to-noise ratio

After the characterization of the geometrical properties of the interferometer system as described above, we investigate the optimal SNR for detecting a SGWB with the two instruments LISA and ET working together. We assume that the two detectors take data approximately for the same amount of time  $T$  (although not necessarily simultaneously, exploiting the stationarity of the SGWB). The optimal SNR for measuring a SGWB with LISA and ET in synergy is built using techniques based on Wiener

<sup>3</sup>The results are obtained by performing the integrations in Eq. (2.13). The integrals contain the relative positions of the interferometer vertices. For definiteness, extending Ref. [29], we set the positions of the LISA interferometer vertices as (with  $L$  being the LISA arm length)

$$\vec{x}_A = \{0, 0, 0\}, \quad \vec{x}_B = L\{1/2, \sqrt{3}/2, 0\}, \quad \vec{x}_C = L\{-1/2, \sqrt{3}/2, 0\}. \quad (2.19)$$

For simplicity, we choose the same arm directions for the triangle forming ET, which of course has much shorter arm lengths. As mentioned above, in this work, we do not consider effects of the relative motion between LISA and ET detectors.

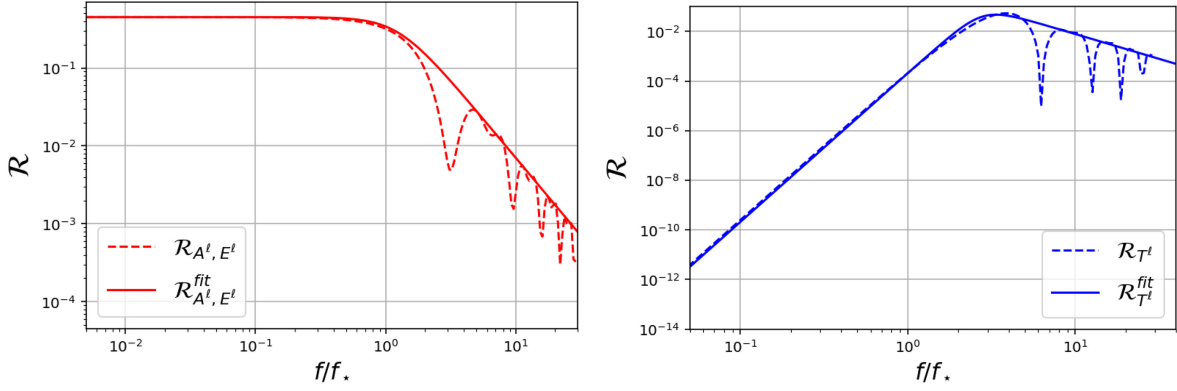


FIG. 1. The numerical LISA response functions for A, E (left panel) and T (right panel) orthogonal channels (dashed lines) as well as the corresponding analytical fits of Eqs. (2.22) and (2.23) (continuous lines).

filtering, combining information obtained from the independent channels  $A^{\ell,e}$  and  $E^{\ell,e}$ . We follow Ref. [29] (see also Ref. [30]), extending it to the general case where we work with two instruments together. Working in the weak-signal limit, denoting with  $S_i$  the signal on each independent channel, with  $N_i$  the noise, and with  $Q_i$  the filter, the SNR in Fourier space reads

$$\text{SNR} = \sqrt{\frac{T}{2}} \frac{\sum_i \int_{-\infty}^{\infty} df S_i(f) Q_i(f)}{\sqrt{\sum_i \int_{-\infty}^{\infty} df N_i^2(f) Q_i^2(f)}}, \quad (2.24)$$

where the sums are over the four channels  $A^{\ell,e}$  and  $E^{\ell,e}$  which are most sensitive to the signal. As mentioned above, the quantity  $T$  indicates the duration of the measurements, which we consider to be comparable in the two experiments. We now wish to determine the optimal filter which maximizes Eq. (2.24). We define a positive definite inner product,

$$(P_i, Q_i) = \sum_i \int_{-\infty}^{\infty} df P_i(f) Q_i(f) N_i^2(f), \quad (2.25)$$

which acts on the four vectors  $(P_i)$ , where  $i = A^{\ell,e}, E^{\ell,e}$ . The SNR can then be expressed as

$$\text{SNR} = \sqrt{\frac{T}{2}} \frac{(S_i/N_i^2, Q_i)}{\sqrt{(Q_i, Q_i)}}, \quad (2.26)$$

and the filter that maximizes the previous expression, up to an overall factor, is  $Q_i = S_i/N_i^2$ . The optimal SNR is (we now integrate over positive frequencies only)

$$\text{SNR} = \left[ T \sum_{i=A^{\ell,e}, E^{\ell,e}} \int_0^{+\infty} df \frac{S_i^2(f)}{N_i^2(f)} \right]^{1/2}. \quad (2.27)$$

We can now decompose the integrand in the previous formula as

$$\begin{aligned} \sum_{i=A^{\ell,e}, E^{\ell,e}} \frac{S_i^2(f)}{N_i^2(f)} &= \left[ \left( \frac{R_{A^{\ell,e}}(f)}{N_{A^{\ell,e}}(f)} \right)^2 + \left( \frac{R_{E^{\ell,e}}(f)}{N_{E^{\ell,e}}(f)} \right)^2 \right] I^2(f) \\ &+ \left[ \left( \frac{R_{A^e}(f)}{N_{A^e}(f)} \right)^2 + \left( \frac{R_{E^e}(f)}{N_{E^e}(f)} \right)^2 \right] I^2(f). \end{aligned} \quad (2.28)$$

It is convenient to assemble the above result as [recall that  $\Omega_{\text{GW}}$  is defined in Eq. (2.4)]

$$\sum_{i=A^{\ell,e}, E^{\ell,e}} \frac{S_i^2(f)}{N_i^2(f)} = \frac{\Omega_{\text{GW}}^2(f)}{\Sigma_{\text{LISA}}^2(f)} + \frac{\Omega_{\text{GW}}^2(f)}{\Sigma_{\text{ET}}^2(f)}, \quad (2.29)$$

with

$$\Sigma_{\text{LISA}}(f) = \left( \frac{4\pi^2}{3H_0^2} \right) f^3 \left[ \left( \frac{R_{A^{\ell,e}}(f)}{N_{A^{\ell,e}}(f)} \right)^2 + \left( \frac{R_{E^{\ell,e}}(f)}{N_{E^{\ell,e}}(f)} \right)^2 \right]^{-1/2}, \quad (2.30)$$

and analogously for the ET.

The result depends on the instrument response  $R$  to the signal and on the noise curve  $N$  for each independent channel. The functions  $\Sigma_{\text{LISA}}(f)$  and  $\Sigma_{\text{ET}}(f)$  are called nominal sensitivity curves—see Ref. [33] for a general discussion—and we represent them in Fig. 2 for the two experiments under consideration. Besides the numerically evaluated sensitivity curves, we also represent analytical approximations for the curves in Fig. 2. The analytical fit we use for LISA is obtained from Ref. [34], while the one for ET is a new result of the present work, and we discuss it in the Appendix. For each experiment, the function  $\Sigma$  encapsulates a weighted combination of response functions and noise on each channel and is useful for visually understanding the sensitivity of the instruments. For an extended discussion on sensitivity curves, see Sec. IV, where we will also discuss the more refined notion of *integrated* sensitivity curves in this context. To summarize,

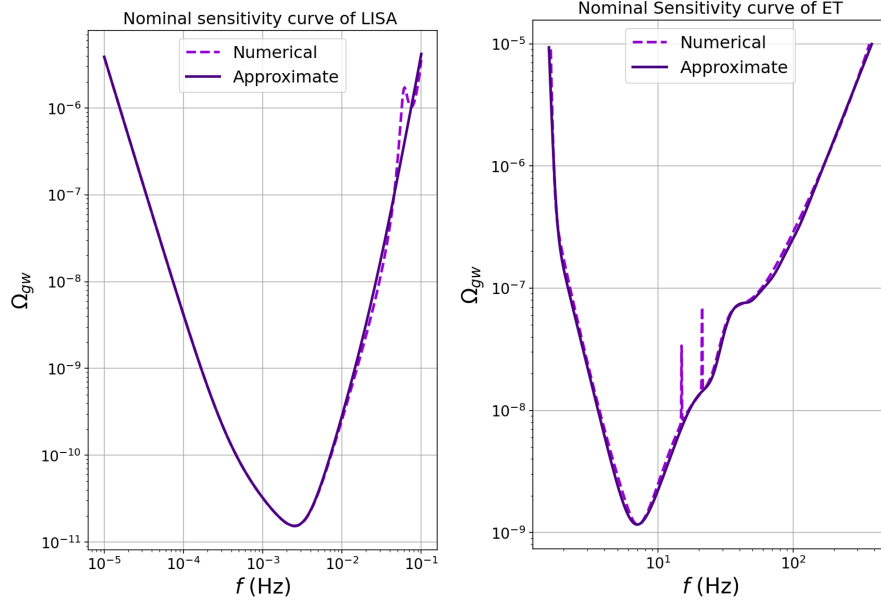


FIG. 2. Nominal sensitivity curves for LISA and the ET. For the latter, we represent the so-called ET-D curve. The approximate analytical fit for ET is discussed in the Appendix. Recall that we take  $h = 0.67$ .

the square of the total SNR is the sum of the squares of the individual SNRs:

$$\begin{aligned} \text{SNR}_{\text{tot}} &= \sqrt{T \int_0^\infty df \left[ \frac{\Omega_{\text{GW}}^2(f)}{\Sigma_{\text{LISA}}^2(f)} + \frac{\Omega_{\text{GW}}^2(f)}{\Sigma_{\text{ET}}^2(f)} \right]} \\ &= \sqrt{\text{SNR}_{\text{LISA}}^2 + \text{SNR}_{\text{ET}}^2}, \end{aligned} \quad (2.31)$$

a formula which will be used in what follows. This expression demonstrates that, by working in synergy, the two detectors can reach higher values of SNR than each experiment operating individually.

Interestingly, the very same results can be obtained in terms of a likelihood function associated with a measurement of  $\Omega_{\text{GW}}$  carried out by the two experiments together. This method is also useful for applications to Fisher matrix forecasts. We assume the structure for the Gaussian likelihood,

$$\begin{aligned} \ln \mathcal{L} &= \text{const} - \frac{1}{2} \int_0^\infty df df' \left( \hat{\Omega}_{\text{GW}}(f) - \Omega_{\text{GW}}^{\text{th}}(f) \right) \\ &\quad \times C^{-1}(f, f') \left( \hat{\Omega}_{\text{GW}}(f') - \Omega_{\text{GW}}^{\text{th}}(f') \right), \end{aligned} \quad (2.32)$$

where  $\hat{\Omega}_{\text{GW}}$  is the measured value and  $\Omega_{\text{GW}}^{\text{th}}$  is the theoretical prediction from various sources for the quantity  $\Omega_{\text{GW}}$  we wish to test. The inverse of the covariance matrix corresponding to the GW measurement by the two experiments together is

$$C^{-1}(f, f') = T \delta(f - f') \left( \frac{1}{\Sigma_{\text{LISA}}^2(f)} + \frac{1}{\Sigma_{\text{ET}}^2(f)} \right). \quad (2.33)$$

Considering  $\hat{\Omega}_{\text{GW}}(f)$  to be the quantity to measure, we can compute the following quantity corresponding to a continuous version of the Fisher matrix:

$$\mathbf{F}(f, f') = - \frac{\delta^2 \ln \mathcal{L}}{\delta \Omega_{\text{GW}}^{\text{th}}(f) \delta \Omega_{\text{GW}}^{\text{th}}(f')} \quad (2.34)$$

$$= C^{-1}(f, f'). \quad (2.35)$$

The optimal SNR can then be computed in terms of a convolution integral:

$$\text{SNR}_{\text{opt}}^2 = \int_0^{+\infty} df df' \Omega_{\text{GW}}^{\text{th}}(f) \Omega_{\text{GW}}^{\text{th}}(f') \mathbf{F}(f, f'). \quad (2.36)$$

Substituting the inverse covariance function (2.33), this result coincides with Eq. (2.31).

The concept of Fisher matrices, of course, can be used more directly to make forecasts on the prospective error bars associated with measured quantities; see, e.g., Refs. [35,36]. Suppose we are interested in measuring the components of a parameter vector  $\Theta_i$ , with  $i$  being an index running over the number of model parameters we are interested in. The corresponding Fisher matrix is

$$\mathbf{F}_{ij} = - \frac{\delta^2 \ln \mathcal{L}}{\delta \Theta_i \delta \Theta_j}, \quad (2.37)$$

where we consider the quantity given in Eq. (2.32) as a likelihood function. Then, the errors on the measurements of  $\Theta_i$  are at least

$$\Delta \Theta_i = \sqrt{(\mathbf{F})_{ii}^{-1}}. \quad (2.38)$$

This is a standard formula that we utilize in later sections. After discussing how to use the two instruments together to measure SGWB signals, in the next section, we will provide motivations and examples of broad multiband SGWB sources, which can benefit from a joint detection by LISA and the ET.

### III. EXAMPLES OF SGWB WITH BROAD FREQUENCY PROFILES

In this section, we discuss examples of cosmological SGWB sources, which are able to produce a broad GW signal with a sizeable amplitude spanning several decades in frequency. We consider, in succession, GW sources from first-order cosmological phase transitions, cosmic strings, and primordial inflation. We are interested in SGWB spectra enhanced within the broad frequency band

$$\mathcal{B}_{\text{tot}} = 10^{-5} \leq f/\text{Hz} \leq 445. \quad (3.1)$$

The lower part of the interval (3.1) corresponds to the region of maximal sensitivity of LISA (mHz), while the upper part corresponds to the region (decahertz) where the ET is more sensitive to a GW signal (see both panels of Fig. 2). We intend to demonstrate that important physical information about the GW source and the Universe's evolution history can be extracted by measuring in synergy the SGWB within the broad frequency interval (3.1).

We are not interested, though, in measuring the finer details of the frequency dependence of the GW spectrum (for methods to do so, see, e.g., Refs. [34,37]). Instead, we wish to characterize the overall frequency profile of the spectrum, including the properties of a SGWB which extends all the way between the lower and the upper regions of the frequency band in Eq. (3.1). A GW spectrum is particularly interesting for us if it has a structure *evolving in frequency* throughout the entire interval (3.1). In such a case, the synergy between the two experiments LISA and ET can be especially useful for better characterizing the signal and extracting its physical properties, compared to measurements made with a single instrument (LISA or the ET). We explore this topic quantitatively by means of Fisher forecasts on the detectability of the properties of the SGWB shape.

A useful SGWB template to keep in mind for the GW energy density of Eq. (2.4), with the properties we need is the so-called *broken power-law* (BPL) function which well describes, at least up to first approximation, GW spectra produced by several early-Universe phenomena [38]. This template applies well to GW spectra from phase transitions and cosmic strings (see Secs. III A and III B). We adopt the frequency shape parametrization of Ref. [39]:

$$\Omega_{\text{GW}}(f) = \Omega_{\star} \left( \frac{f}{f_{\star}} \right)^{n_1} \left[ \frac{1}{2} + \frac{1}{2} \left( \frac{f}{f_{\star}} \right)^{\sigma} \right]^{\frac{n_2 - n_1}{\sigma}}. \quad (3.2)$$

The quantities  $f_{\star}$  and  $\Omega_{\star}$  in Eq. (3.2) control the position of the break and the amplitude of the spectrum around the break. The quantities  $n_{1,2}$  are related to the spectral indices before and after the break, while  $\sigma$  controls the smoothness of the break—the smaller  $\sigma$  is, the smoother the transition is. If the break occurs somewhere the middle of band (3.1), it will be interesting to detect it with the two experiments in synergy for the possibility of measuring both the indices  $n_1$  and  $n_2$ .

If  $n_1$  and  $n_2$  have opposite sign, the break position  $f_{\text{break}}$  and the corresponding value of  $\Omega_{\text{GW}}^{\text{break}}$  are given by

$$f_{\text{break}} = (-n_1/n_2)^{1/\sigma} f_{\star}, \quad (3.3)$$

$$\Omega_{\text{GW}}^{\text{break}} = \Omega_{\star} \left[ \frac{(-n_2/n_1)^{n_1/(n_1-n_2)}}{2} + \frac{(-n_1/n_2)^{n_2/(n_2-n_1)}}{2} \right]^{(n_2-n_1)/\sigma}. \quad (3.4)$$

Currently, we have an indirect bound on the amplitude of a cosmological SGWB signal in the frequency band (3.1) because its amplitude should not exceed the BBN bound  $\Omega_{\text{GW}} \leq 1.7 \times 10^{-6}$  [40]. Moreover, at the frequency scales of ground-based interferometers—around decahertz—the LIGO-Virgo-KAGRA Collaboration currently sets the upper bound  $\Omega_{\text{GW}} \leq 6 \times 10^{-8}$  at the reference ground-based frequency of 25 Hz [41], for a flat GW spectrum. In this work, we consider the BBN bound as reference for the maximal amplitude of the SGWB even when studying GW sources active after BBN.

After these preliminary considerations, we can start looking at concrete early-Universe sources of GW. We do not plan to be exhaustive but to discuss selected examples of sources which lead to a broad GW spectrum, whose detection would benefit from synergies between LISA and the ET. We focus on the theoretical aspects of the discussion and also present Fisher estimates on the capability of the two instruments together to better detect properties of the SGWB profile. Although the template (3.2) is simple and general enough to accommodate several early-Universe sources—as discussed in Secs. III A and III B—for selected cases in the context of inflation, we go beyond the profile of Eq. (3.2), and we consider a different broad ansatz for  $\Omega_{\text{GW}}$ —the so-called log-normal profile—to better describe the frequency dependence of the SGWB (see Sec. III C).

#### A. Cosmological phase transitions

Several well-motivated models of particle physics predict the existence of scalar sectors beyond the Standard Model, whose potentials are characterized by local minima. The energy release of strong first-order phase transitions (PTs) between different vacua produces a stochastic background of GW. The detection of such a background would provide invaluable information on physics beyond the

Standard Model and on the early cosmic evolution of our Universe. We refer to Refs. [17,39,42,43] for complete discussions and reviews on PT and their consequences for different aspects of GW production. There are essentially three mechanisms<sup>4</sup> for GW production: collisions among bubbles of different vacua [45–47], sound waves in the primordial plasma [48,49], and turbulent motion [50–52]. The resulting shape in frequency of the SGWB spectrum has a characteristic peak structure associated with the duration and properties of the PT responsible for the GW emission. The SGWB from strong first-order PT increases from small toward large frequencies, reaches a maximum associated with the Hubble size during the PT in the early Universe, and then decreases in amplitude.

According to the recent discussion in Ref. [39], in the first case of bubble collisions, we can expect a SGWB with a broken power-law profile as in Eq (3.2), while the other two cases are better described by a double broken power-law template. At first approximation—since as mentioned earlier we are not interested in fine details of the SGWB frequency dependence but only on its overall structure within the broad interval (3.1)—we do not take into account the differences between the latter and the former template. We consider the BPL profile in Eq. (3.2) as describing reasonably well the overall frequency dependence of a SGWB from first-order PT, which can in principle span over the frequency band (3.1). In this context, the parameters in the template (3.2) depend on the GW production mechanisms as well as on the particle physics models sourcing the PT in the first place (see the recent work [39] for a more detailed analysis).

### 1. Position and height of the peak

For the case of bubble collisions, many studies over the years have clarified the role of bubble dynamics and surrounding relativistic fluid shells for GW production (see, e.g., Ref. [43], which contains a complete review). The dynamics of fluid shells might be important, requiring going beyond the so-called thin-shell approximation (see Refs. [53,54] for latest developments). In the limit of strong phase transitions, the inverse duration of the transition, denoted as  $\beta/H_*$  (normalized against the Hubble parameter at the transition epoch), and the temperature  $T_*$  at transition are related to the BPL amplitude  $\Omega_*$  and break position  $f_*$  by the formulas [39]

$$\Omega_* \simeq \frac{2H_*^2}{10^6 \beta^2}; \quad \frac{f_*}{\text{Hz}} \simeq \frac{1}{10^8 \sqrt{\Omega_*}} \left( \frac{T_*}{100 \text{ GeV}} \right). \quad (3.5)$$

We refer to Ref. [39] for details. Hence, by tuning appropriately the transition temperature and its duration,

<sup>4</sup>Recently, Ref. [44] pointed out a fourth source, namely, particle production from bubbles sources GW during first-order PT.

the position of the break [see Eq. (3.3)] might be placed freely within the band (3.1).

A precise measurement of the value of  $f_{\text{break}}$  informs us of when the PT occurs during cosmological history and the timescale of its duration. For an explicit example, let us assume  $n_1 = -n_2 \geq 0$  (so that  $f_{\text{break}} = f_*$ ) and a high SGWB amplitude  $\Omega_* = 10^{-6}$ . The transition temperature corresponds to the electroweak value— $T_* = 10^2$  GeV—for a break in the LISA band at  $f_* = 10^{-5}$  Hz, the lower extremum of the interval (3.1). On the other hand, we find an intermediate scale of  $T_* = 10^9$  GeV for a break within the ET band at  $f_* = 5 \times 10^2$  Hz, the upper extremum of the interval (3.1) (see the recent discussion in Ref. [55]). Such intermediate-case PTs are very well motivated from scenarios of BSM involving axion physics with classic Peccei-Quinn symmetry breaking scales around  $10^9$ – $10^{11}$  GeV [56–59]. Interestingly, for this first-order PT, the energy scale of new physics the ground-based detectors are sensitive to, roughly coincides with the lowest possible energy scale at which the Peccei-Quinn (PQ) symmetry  $U(1)_{\text{PQ}}$  has to be broken in QCD axion models which also address the strong  $CP$  problem of the SM [60–63]. The involved axion scalar field is a viable cold DM candidate [64–66], and even more generally, axionlike particles are well motivated, since they are naturally present as pseudo Nambu-Goldstone bosons in many BSM extensions with a spontaneously broken global  $U(1)$  symmetry, e.g., in several string theory avatars [67–69]. Yet another motivation for intermediate-scale PT comes from neutrino mass generation also known as seesaw mechanism connected to the scale of baryogenesis via leptogenesis; see, e.g., Refs. [70–74]. In fact, while standard thermal leptogenesis is a simple and elegant mechanism, it requires a small window of right-handed neutrino masses in the high-energy regime  $10^9$ – $10^{11}$  GeV. Hence, GW detectors could probe these energy ranges which cannot be probed by accelerator experiments (see the analysis in Ref. [75] in terms of existing GW data).

Moreover, it is also possible to push  $T_*$  to high values considering nonminimal Higgs scenarios, or scalar setups belonging to dark sectors beyond the Standard Model (see, e.g., Ref. [76], and also see Ref. [77] for an early, complete analysis of the possibility of tuning the scale of the transition to intermediate values and its consequences for interferometer detections and physics beyond the standard model). The possibility of detecting a break in the spectrum somewhere within the entire range (3.1) would be an important opportunity to study the physics of PTs and probe high-energy physics beyond the electroweak scale.

### 2. The spectral indices and our benchmark scenarios

Interestingly, the values of the tilts  $n_{1,2}$  and of the smoothing quantity  $\sigma$  depend more specifically on the PT scenario and GW source under consideration.

TABLE I. Benchmark values for the scenarios corresponding to cosmological phase transitions.

	$\Omega_\star$	$n_1$	$n_2$	$\sigma$	$f_\star$
PT1	$1 \times 10^{-10}$	3	-1	7.2	0.04
PT2	$1 \times 10^{-8}$	2.4	-2.4	1.2	0.2

Measuring both indices  $n_1$  and  $n_2$  accurately is then essential to reconstruct the details of the physics leading to the PT: such a measurement can be achieved by the synergy of LISA and the ET, as we are going to demonstrate. We analyze two benchmark scenarios, PT1 and PT2, as summarized in Table I. For uncorrelated primordial sources, one finds a slope  $n_1 = 3$  in the deep infrared (see, e.g., Ref. [78] for a detailed analysis). But more generally, the slope depends sensitively on the GW production. We first consider a benchmark scenario PT1, with spectral index  $n_1 = 3$  in the infrared; in the UV, we consider  $n_2 = -1$  as predicted in scenarios where GWs are produced by sound waves of the bubble surrounding plasma or by effects of turbulent behavior in the fluid. For the second benchmark scenario, PT2, we consider the model of Ref. [79] in the context of highly relativistic fluid shell dynamics, which finds  $n_1 = -n_2 \simeq 2.4$  and  $\sigma \simeq 1.2$ . These two scenarios are presented in the left panel of Fig 3.

### 3. What can we learn about PT by LISA and the ET in synergy?

In both of the aforementioned benchmark models, the position of the break of the broken power-law spectrum is

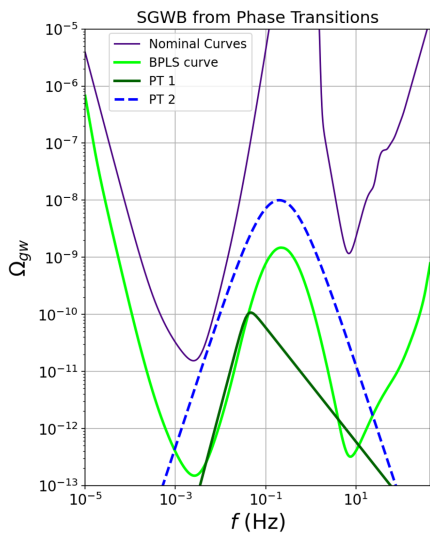


FIG. 3. Examples of SGWB from phase transitions (PT); see Sec. III A. The purple curves correspond to the LISA and ET nominal curves, the green curve corresponds to the integrated sensitivity curve for broken power-law scenarios discussed in Sec. IV, and the blue and green lines represent the benchmark scenarios in Table I.

located somewhere in the middle between LISA and ET bands; see Fig. 3. The plots suggest that a measurement in synergy between LISA and ET would allow us to get important information on the position of the break and the value of the spectral tilts, and thereby on particle physics models leading to a first-order PT. Notice that, importantly, the signal profile lies well below the nominal sensitivity curve of both experiments. Nevertheless, it can be detected by integrating over frequencies: recall the expression for the SNR [Eq. (2.27)]. Such an integration allows one to acquire sufficiently high values of SNR even if the signal lies well below the nominal sensitivity curves of the experiment. In fact, this property suggests the definition of broken power-law sensitivity curve, as depicted with light green color in Figs. 3 and 5, left and middle panels: the GW signals lie well above such a curve. We will reconsider this topic in Sec. IV, in the context of frequency-integrated sensitivity curves.

In fact, we can carry out a Fisher analysis using a likelihood whose structure is given in Eq. (2.32) and assuming the BPL ansatz (3.2) with the aforementioned two sets of benchmark values for the parameters, summarized in Table I. The benchmark values of  $\Omega_\star$  are selected in a such a way as to show how the two instruments *together* can achieve good accuracy in the measurements of the template parameters. The results are shown in Fig. 4. From now on, we will present Fisher plots obtained using the GetDist package [80].

For both the scenarios PT1 and PT2 as shown in Fig. 4, each of the two experiments—LISA and the ET—can measure with good accuracy *only one* of the two spectral indices  $n_1$  or  $n_2$ . The two experiments in synergy, though, can measure *both* these quantities well, with an accuracy of at least 10%. Apart from the spectral indices, the parameter  $\sigma$  controlling the degree of smoothness of the transition can also be measured accurately by the synergy of the two experiments. This implies that, by working with LISA and the ET together, we can obtain much richer information on the physics of PT occurring at high temperature scales. Additionally, for both scenarios, the ET experiment by itself cannot accurately measure the amplitude of the SGWB. Only in synergy with LISA can it do so, measuring with a 10% accuracy all the parameters characterizing our benchmark models. Moreover, the synergy of the two experiments can help in alleviating degeneracies in the parameter measurements—see, for example, the measurement of  $\sigma$  and  $\Omega_\star$  by the ET only in the second row of Fig. 4.

The correlations, shown by the ellipses, are an indication of how the parameters covary according to the constraints on LISA or the ET. Let us first consider the case of PT1. We can estimate that the break in the signal occurs at a frequency of approximately 0.046 Hz, which is within the LISA band. This break is farther within the LISA band than in the case of PT2, wherein the break occurs around 0.2 Hz.

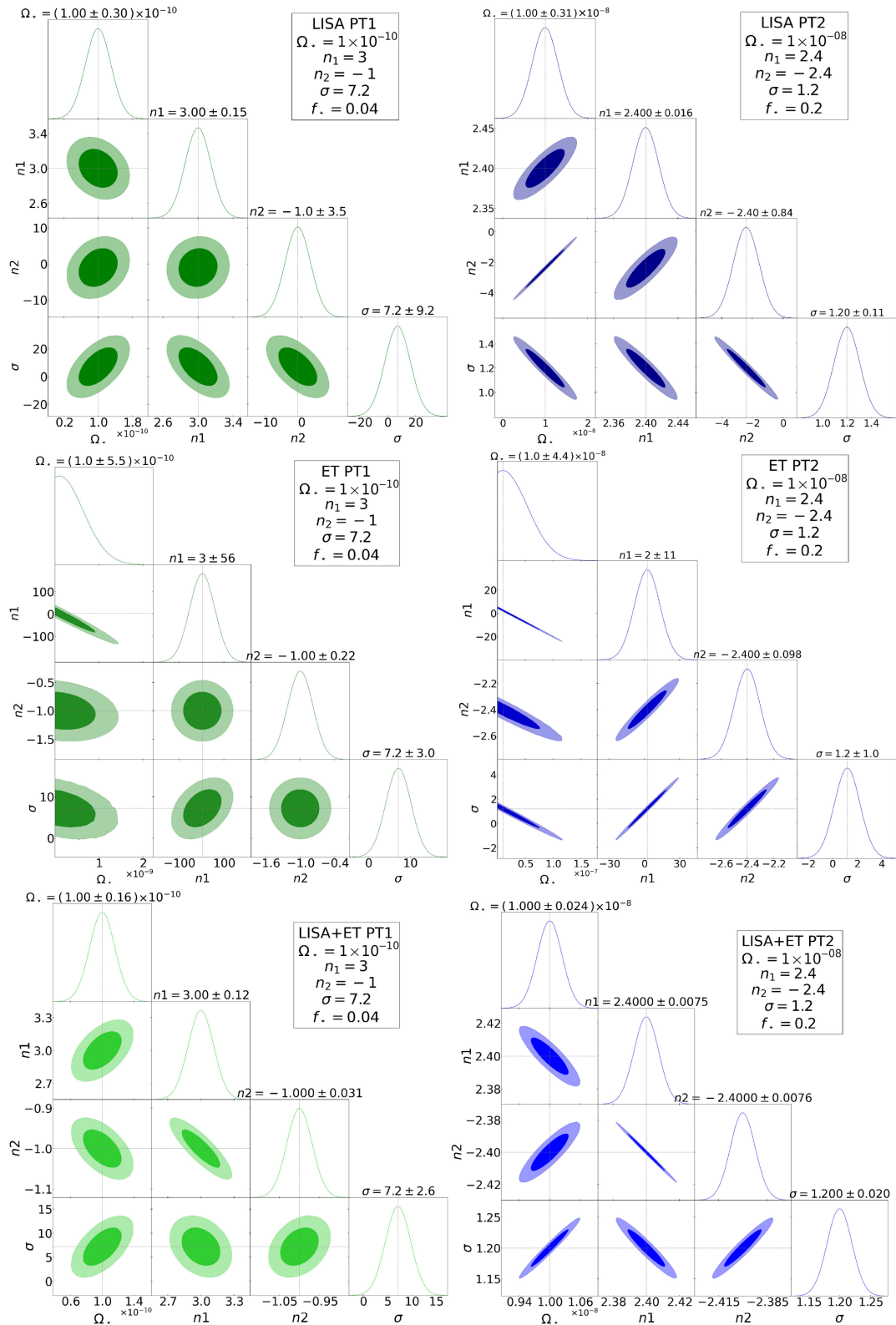


FIG. 4. Fisher forecasts for the phase transition benchmark scenarios PT1 and PT2, summarized in Table I.

Therefore, the ET cannot effectively constrain  $\sigma$  or  $n_1$  on its own. Moreover, due to the low amplitude of the signal and the resultant low SNR, even LISA is unable to

constrain the quantity  $\sigma$  well. ET mainly gathers its SNR from the part of the signal after the break. If this part of the signal becomes steeper—that is, if  $n_2$  becomes a

TABLE II. Calculated SNR values for the scenarios corresponding to cosmological phase transitions.

	LISA	ET	LISA + ET
PT1 SNR	11	13	17
PT2 SNR	528	544	758

larger negative number—then in order to compensate for this fact and accumulate adequate SNR, the amplitude of the signal should become larger. This behavior is manifest in the correlation between  $n_2$  and  $\Omega_\star$  for the ET. Considering the combination LISA + ET, if the slope  $n_2$  alone become steeper, the total SNR decreases. Because of the low overall amplitude of the signal, making  $n_2$  very steep could result in the total SNR falling below the value of 5, the minimum SNR value we consider in this work for the detectability of a signal. Hence, the  $\Omega_\star$  has to increase, for allowing for the total SNR to cross such a threshold value.

To elucidate this point further, we consider the case of PT2 also. As mentioned earlier, in this case, the break in the signal occurs within the LISA band, around 0.2 Hz. Because of the relatively higher amplitude of the signal compared to PT1, LISA by itself can constrain  $n_1$  and  $\sigma$  quite well. However, the ET cannot constrain sufficiently well either of these parameters on its own. Considering the case of ET only, if the part of the signal after the break becomes steeper—that is, if  $n_2$  becomes a large negative number—then the signal amplitude has to become larger in order to compensate for this fact and accumulate adequate SNR. This is what we learn in the correlation between  $n_2$  and  $\Omega_\star$  for the ET. Such behavior is similar to what we find for PT1. However, when considering the combination LISA + ET—which includes adequate SNR from the LISA band—by increasing  $\Omega_\star$ , we would increase the total combined SNR to very large values, even though the SNR for the ET alone might remain the same. Therefore, the correlation pattern is reversed. We see that the SNR for PT2 is much higher with respect to PT1. The values are 42 to 48 times larger for PT2 than for PT1, (see Table II). In conclusion, this analysis demonstrates quantitatively, by means of the Fisher plots of Fig. 4, the advantages of measuring the profile of SGWB over a broad interval, for reconstructing the physics of the PT and the details of the frequency profile around the peak.

## B. Cosmic strings

Another opportunity for determining the pre-BBN cosmic history of the Universe is associated with the detection of GW sourced by a network of cosmic strings. Cosmic strings are basically one-dimensional objects produced by the spontaneous breaking of a  $U(1)$  symmetry in the early Universe [81,82] or sometimes considered as fundamental objects, for instance, in superstring theory [83–87]. The

essential feature in the GW emitted by the cosmic strings is that they are sources of very long-standing over the entire history of the evolution of the Universe [88–93]. Let us try to understand why; after the formation of the network of cosmic strings, it assumes a constant fraction of the total energy budget of the Universe, and this is very popularly known as the scaling regime [94–99]. Consequently, as long as the strings exist in the Universe, it will keep on emitting GW during the scaling regime and this happens through most of the Universe’s history. Since the frequency of cosmic sources of GW represents time in the early Universe (higher frequency means earlier time), this generates a GW spectrum spanning many orders of magnitude in frequencies. Therefore, a possible measurement of the GW spectrum from high to lower frequencies will determine the Universe expansion rate from early to later times by investigating the features on the cosmic string GW spectrum [100–105]. A detailed study of the impact of various pre-BBN cosmological epochs on the GW spectrum emitted from local and global cosmic strings was carried out in Ref. [105], which clearly predicts the multiband frequency spectrum of the GW detectors. In fact, the SGWB from cosmic strings can be conveniently studied in synergy between LISA and ET. (See, e.g., Refs. [106,107] and references therein for a recent assessment in the context of LISA physics.)

The process of string loop formation, evolution, and decay into GWs is quite complex. It is usually studied numerically, although accurate semianalytical fits for the frequency shape of the SGWB can be determined (see, e.g., the recent account [107]). The SGWB characteristics depend on the string tension ( $G\mu$ ), normalized against the gravitational constant  $G$ , and on the loop size  $\alpha$ , normalized against its time of formation. Typically, the SGWB frequency profile initially increases during the first phase of the decay of string loops into GWs, up to a maximum at the frequency [38]

$$f_{\max} \simeq 3 \times 10^{-8} \left( \frac{G\mu}{10^{-11}} \right)^{-1} \text{ Hz.} \quad (3.6)$$

The value of the quantity  $G\mu$  is quite model dependent, but  $f_{\max}$  usually occurs at frequencies well below the band (3.1) we are interested in. For example, for a specific model of loop distribution, the LIGO-Virgo-KAGRA Collaboration sets a bound  $G\mu \leq 4 \times 10^{-15}$  [108]. Then, at larger frequencies, the SGWB becomes nearly constant, or slightly decaying with an approximately constant slope. We refer the reader to Ref. [38] for a more complete discussion and references therein. As a consequence, if future measurements favor a SGWB entering from the left side of the band (3.1) with a negative slope, they will provide circumstantial evidence for a cosmic string origin of the signal. Going beyond the discussions of local cosmic strings as above, there are several additional instances of CS sources such as metastable cosmic strings [109], global

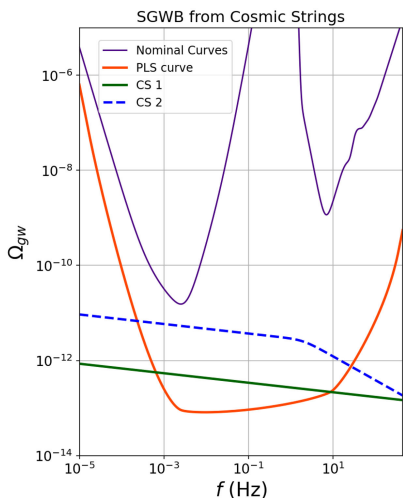


FIG. 5. Examples of SGWB from cosmic strings (CS); see Sec. III B. The purple curves correspond to the LISA and ET nominal curves, the green curve corresponds to the integrated sensitivity curve for broken power-law scenarios discussed in Sec. IV, and the blue and green lines represent the benchmark scenarios in Table III.

cosmic strings [110] or cosmic superstrings [111], current-carrying [112] and superconducting strings [113]. Various other topological defects like monopoles and textures can interact with cosmic strings [114]; a separate dedicated analysis would be required since for each of them carries features of top of the standard flat spectrum, which can be tested and searched for in the broad band interval of Eq. (3.1).

Motivated by the previous considerations, we shall now discuss two benchmark models. In our first cosmic string benchmark scenario—CS1—we assume a constant power-law profile in the frequency band (3.1), with a spectral index  $n_1 = -0.1$ . If the amplitude of  $\Omega_{\text{GW}}$ , proportional to  $(G\mu)^2/H_0^2$ , is sufficiently large, then such a power-law profile can be probed with both the LISA and the ET instruments. We present this case in Fig. 5. Note that the constant slope lies well below the nominal sensitivity curves. Nevertheless, as mentioned above, it can be detected with sufficient SNR by integrating over frequencies. For this reason, we represent in the same plot in light green the corresponding broken-power-law sensitivity curve, more on this in the next section.

Let us also consider another interesting possibility offered by the synergy of LISA with the ET, an accurate test of the early expansion of our Universe. By measuring the frequency profile of the spectrum, we can probe (or constrain) early epochs of nonstandard cosmic expansion, preceding big bang nucleosynthesis. Early matter domination eras, kination domination, or the early presence of extra degrees of freedom beyond the Standard Model can modify the string network evolution, and the corresponding dynamics of GW production (see, e.g., Ref. [115] and references therein for a comprehensive review and Ref. [105] for a dedicated analysis).

TABLE III. Benchmark values for each cosmic string scenario.

	$\Omega_*$	$n_1$	$n_2$	$\sigma$	$f_*$
CS1	$4 \times 10^{-13}$	-0.1	-0.1	...	0.02
CS2	$2.5 \times 10^{-12}$	-0.1	$-\frac{1}{2}$	3	2

Nonstandard early cosmological epochs lead to sudden changes, as breaks and features in slope at frequency<sup>5</sup> [38]

$$f_{\text{break}} \simeq (9 \times 10^{-3} \text{ Hz}) \left( \frac{T_{\text{RD}}}{\text{GeV}} \right) \left( \frac{10^{-12}}{\alpha G\mu} \right)^{1/2}. \quad (3.7)$$

By making appropriate choices of the string network properties, the break position can occur within the interval (3.1). Right after the break, the slope of the spectrum changes to a slope depending on  $\omega$ —the equation of state during the nonstandard cosmological expansion. For  $\omega \geq 1/4$ , the tilt  $n_2$  is given by  $n_2 = -2(3\omega - 1)/(3\omega + 1)$  [107]. Hence, knowledge of the spectral tilts  $n_{1,2}$  and of the break position  $f_{\text{break}}$  offers us crucial information not only on the cosmic string properties but also on the evolution of the Universe prior to BBN. In Fig. 5, we show an explicit example of this phenomenon for the benchmark scenario dubbed CS2 in Table III, where we have chosen  $\omega = 5/9$ .

Other than continuous symmetries which when broken leads to GW (as discussed above), domain walls (DWs) [116] are topological defects and are formed when a discrete symmetry in some BSM scenario is broken after inflation. As is well studied, during the scaling regime when the DW network evolves and expands along with its surroundings, the energy density stored is  $\rho_{\text{DW}} = c\sigma H$  [82,117], where  $\sigma$  is the surface tension of the wall and  $c = \mathcal{O}(1)$  is a scaling parameter. DWs keep on emitting GWs until they annihilate at a temperature given by  $T = T_{\text{ann}}$  [118–121]. The peak frequency of the resulting GW spectrum from DW annihilation tells us about the horizon size at the time of DW annihilation,  $f_{\text{peak}} = f_H(T_{\text{ann}})$ . Another important feature is that for frequencies  $f \gg f_{\text{peak}}$  the amplitude of the GW spectrum scales as  $f^{-1}$ . Studying closely, the approximation for the GW spectrum at the formation time takes the form  $T = T_{\text{ann}}$  are shown in Refs. [117,122], from which it can be understood the GW spectrum depends on  $\alpha_* \equiv \rho_{\text{DW}}(T_{\text{ann}})/\rho_r(T_{\text{ann}})$ , which is the energy density in the domain walls relative to the radiation energy density  $\rho_r$  of the Universe at the time of DW annihilation. The microscopic physics parameters of the DW model are the relative energy density in DWs,  $\alpha_*$ , and the temperature at which they annihilate,  $T_{\text{ann}}$ . Depending upon if the DWs

<sup>5</sup>Here,  $T_{\text{RD}}$  is the Universe temperature at the transition between nonstandard evolution and radiation domination. We do not take into account in this formula possible effects of extra degrees of freedom beyond the Standard Model active at early epochs.

annihilate completely into dark radiation or into visible sector radiation (SM radiation), the energy density can be constrained as the equivalent number of neutrino species [122]  $\Delta N_{\text{eff}}$ , which is constrained by BBN ( $\Delta N_{\text{eff}} < 0.33$ ) [123] and CMB ( $\Delta N_{\text{eff}} < 0.3$ ) [124,125].

We point out that the symmetry-breaking scale probed by GW in this context is different than in PT scenarios, due to the different microscopic physics involved; see comparative analysis in Ref. [126].

### 1. What can we learn about CS from synergies between LISA and the ET?

The two benchmark scenarios CS1 and CS2—a single power law and a broken power law—are summarized in Table III. Again, the value of  $\Omega_{\star}$  in the two cases (and  $f_{\star}$  in CS2) are selected with the aim of demonstrating the advantages offered by the synergy of the two instruments. The corresponding Fisher analysis is collected in the plots in Fig. 6. Similar to the case of phase transitions, this plot demonstrates the advantages of synergetic measurements with the two experiments for accurately measuring the parameters of each benchmark scenario. Only the two instruments together can measure with a 10% accuracy the entire set of parameters. Moreover, a detection in synergy can reduce apparent degeneracies characterizing the detection with single instruments for the case CS1 (see Fig. 6, first row).

## C. Cosmological inflation

Cosmological inflation is a well-studied early Universe phenomenon capable of producing a stochastic background of gravitational waves (see, e.g., Ref. [127] for a textbook account). While the simplest models of inflation predict a SGWB amplitude too small to be detected by LISA, there are several well-motivated scenarios capable of raising the amplitude of the spectrum to an observable level within the band (3.1). These scenarios are based on multiple field dynamics involving vector and axion fields [128,129], spontaneous breaking of space-time symmetries [130–132], or secondary effects associated with primordial black hole production (PBH) [133,134] (for reviews, see, e.g., Refs. [135,136]). Various inflationary sources can provide distinct frequency profiles for  $\Omega_{\text{GW}}$ , which can be distinguished when detected by GW experiments. In general, the frequency profile of a SGWB produced by inflation is much richer in features than SGWB produced by other phenomena, and it cannot be described by the broken power-law ansatz of Eq. (3.2). It may include a log-normal profile, multiple peaks, or shapes characterized by oscillatory features (see, e.g., Ref. [137] for examples, and a classification of SGWB templates suitable for describing GW from different inflationary scenarios). Moreover, quite interestingly, the SGWB characteristics depend on the very early cosmological history preceding BBN, which are imprinted in the SGWB frequency spectrum. Hence, before focusing on developing forecasts to detect a specific template of

inflationary SGWB by means of synergies of LISA and the ET, we theoretically further motivate how frequency profiles of SGWB originating from inflation—more general than Eq. (3.2)—may provide information on the early Universe evolution prior to BBN.

### 1. Inflationary first-order tensor perturbations

The primordial spectral index  $n_T$ , defined in terms of log derivative of the power spectrum along the momentum scale, is a crucial quantity for characterizing the inflationary primordial tensor power spectrum. Standard single-field slow-roll inflation models predict a red-tilted spectrum, with  $n_T$  satisfying the slow-roll consistency relation  $n_T \approx -r/8$  [138]. However, there exist several more complex scenarios characterized by blue-tilted spectra ( $n_T > 0$ ), originating from various cosmological models involving high energy scales [139–146]. Since the primordial GW background, after being produced during inflation, exists all throughout cosmic history, the spectrum is a perfect target for the multiband frequency study we carry on in our analysis.

Just like the GW spectrum from cosmic strings, GW from inflation are also ideal targets for probing the period of pre-BBN history, i.e., the Universe barotropic parameter  $w$  in the postinflationary era. Let us discuss some examples where the background equation of state deviates from the standard prediction for radiation domination ( $1/3$ ). We can consider models of quintessential inflationary theories [147–150], or nonoscillatory inflation models [151]. In these cases, the scalar field (the inflaton or some spectator field) keeps rolling for a long time even after inflation ends. As a consequence of this process, the primordial Universe experiences a phase known as *kination* [152,153], during which the scalar kinetic energy fraction becomes the dominant component of energy budget in the Universe. This phase is not too long lasting, as the corresponding energy decreases fast as  $\rho_{\phi} \propto a^{-6}$  before the onset of the standard radiation-domination phase. The corresponding background equation of state during kination is given as  $w = 1$ , stiffer than the barotropic parameter during radiation-dominated (RD) ( $w = 1/3$ ) or during matter domination ( $w = 0$ ). Inflationary tensor perturbations reentering the horizon during this phase receive a boost in their amplitude with respect to modes reentering the horizon during RD. See, e.g., Refs. [154–160]. More in general, we can consider a stiff era when the barotropic parameter of the Universe lies in the range  $1/3 < w < 1$ . Such phenomena were investigated in Ref. [161], finding that in order to get a detectable signal in LISA the stiff period in the postinflationary epochs must be in the range  $0.46 \lesssim w \lesssim 0.56$  with a high inflationary scale  $H_{\text{inf}} \sim 10^{13}$  GeV and the reheating temperature in the range  $1 \text{ MeV} \lesssim T_{\text{reh}} \lesssim 150 \text{ MeV}$  assuming no blue-tilting ( $n_T \sim 0$ ). A realization of this possibility in UV-complete inflationary models was actively studied in details in Refs. [162,163] along with other interesting predictions. Moreover, subsequent

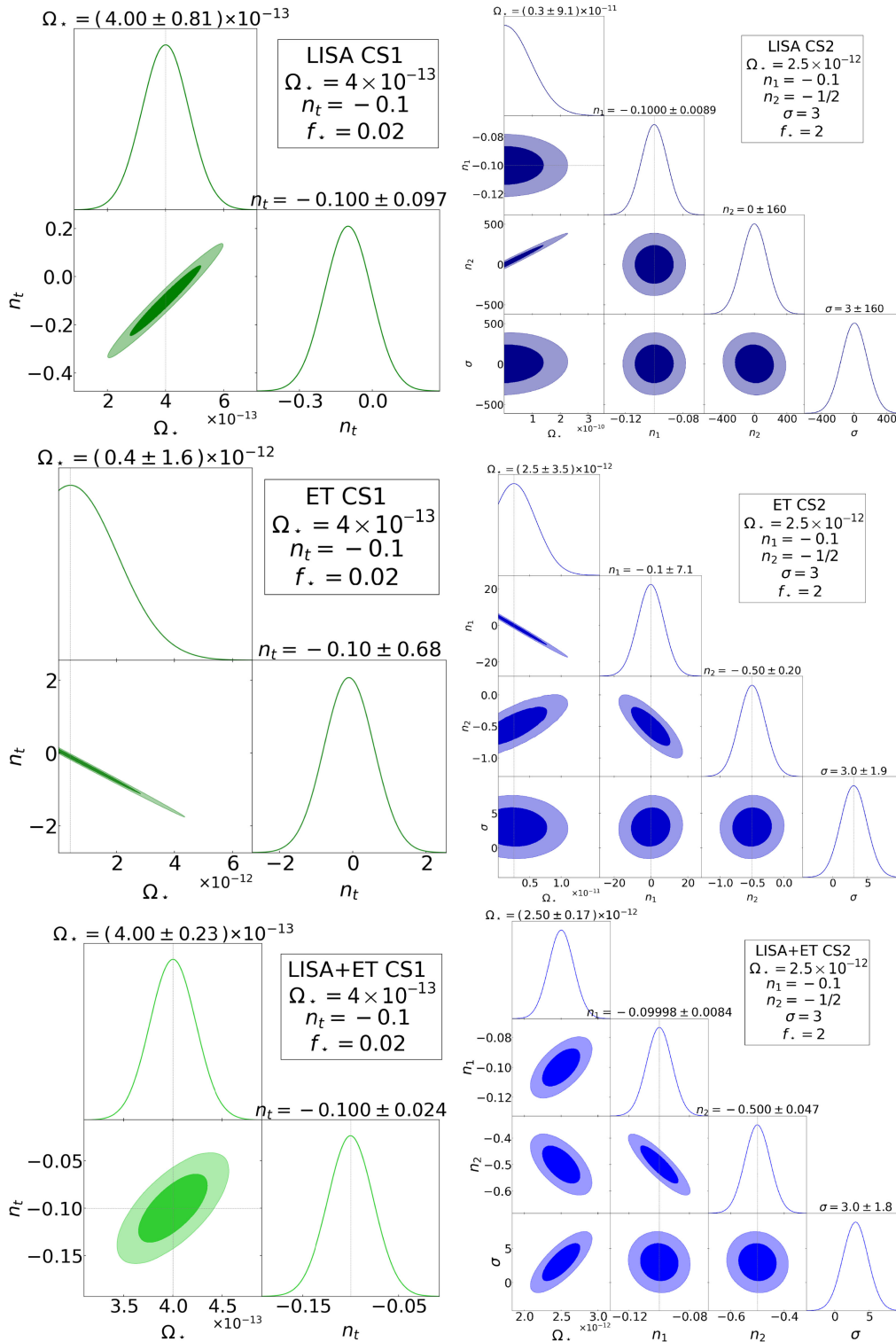


FIG. 6. Fisher forecasts for the cosmic string benchmark scenarios CS1 and CS2, as summarized in Table III.

cosmological eras can imprint signatures on the resulting GW spectrum [114,153,155,157,164,165]. Other well-studied examples of such scenarios include: a long-lived heavy scalar field generating an early matter era [103,115,166–171]; a very fast rolling scalar field

generating a kination era [147,153,156,165,172–176]; a supercooled phase transition [70,177–186]; an extended particle physics sector undergoing decays and scatterings, or a broad distribution of PBHs evaporating in the early Universe, as studied in detail in Refs. [187–191].

## 2. Scalar-induced GW

Yet another important and well studied source of cosmological GWs is the so-called scalar induced SGWB (second-order tensor perturbation) [133,134,192–195] particular with boosted interests in very recent times [196–220] due to the connection with dark matter in the form of primordial black holes.

Just as for the cosmic strings or the first-order inflationary GW, the induced SGWB is also a very well-recognized tool to test the thermal history of the Universe but leading to different spectral shapes controlled by different aspects of microphysics. Reference [215] extends the investigations of the induced SGWB for radiation-dominated and early matter-dominated Universes to more arbitrary barotropic parameters  $w > 0$  and predicts a multiband GW frequency spectrum including motivations for primordial black hole domination and its evaporation [190,191]. In Ref. [215], it is shown that for an adiabatic perfect fluid the shape of the peak of the spectrum depends on the value of  $w$ . Along similar lines, Ref. [221] shows the impact in the GW spectrum due to the change in the effective degrees of freedom in thermal history, like those occurring during the QCD and electro-weak phase transitions in the early Universe. In a more general setup, Ref. [222] shows that the infrared side of the GW spectrum has a universal slope given a certain  $w$ .

The broad frequency profile of scalar induced GW is related with the epochs at which the high-density scalar fluctuations reenter the horizon (and may collapse to form PBH). In this manner, scalar-induced GWs probe the thermal history of the Universe; see Ref. [223]. We remark that the difference between this probe of cosmic history with that of inflationary first-order and cosmic strings lies in the shape of the resultant GW spectrum as well as the microphysics involved.

## 3. Particle production during and after inflation

Axion or more general pseudoscalar inflation models with particle production [224–237] are characterized by a pseudoscalar inflaton  $\chi$  which respects an approximate shift symmetry [231] and a Chern-Simons coupling of the form  $\chi F\tilde{F}$  to a  $U(1)$  gauge field.  $F$  denotes the field strength of the gauge field, and  $\tilde{F}$  is its dual. Such Chern-Simons couplings lead to a tachyonic production of a transverse mode of the gauge fields generating a boosted primordial GW spectrum [128,144,238–252]. Going beyond axion inflation setup, even in models in which an axion or an axionlike particle is not the inflaton, a SGWB can be produced [253–259]. After the axion starts rolling, it induces a tachyonic instability for one of the dark photon helicities, causing vacuum fluctuations to grow exponentially. This effect generates a time-dependent anisotropic stress in the energy-momentum tensor, which ultimately sources the tensor perturbations. The GW formation ends when the tachyonic band closes at temperature  $T_* \approx \frac{1.2\sqrt{m_a M_{\text{Pl}}}}{g_*^{1/4}(\alpha\theta)^{2/3}}$

where  $\alpha$  is the coupling with the dark photon,  $\theta$  is the initial misalignment angle, and  $m_a$  is the mass of the axion [253]. For well-motivated and suitable values of axion mass and coupling, we can get a broad multiband frequency profile detectable by LISA and the ET; see Eq. (3.8).

## 4. Our ansatz

After discussing theory motivations aimed at underlying how the detection of GW from inflation can help in characterizing the thermal history of the Universe, we now focus on forecasting the detectability of a specific SGWB template, with a log-normal profile,

$$\Omega_{\text{GW}} = \Omega_* \exp\left[-\frac{\ln^2(f/f_*)}{2\rho^2}\right]. \quad (3.8)$$

The previous equation is characterized by three free parameters:  $\Omega_*$ ,  $f_*$ , and  $\rho$ . These parameters control the amplitude, position, and sharpness of the peak, respectively. The log-normal ansatz (3.8) is qualitatively different from the BPL profile of Eq. (3.2). The SGWB profile of Eq. (3.8) can be generated by the axion or axion spectator models of inflation [260–262] described above. Hence, it is theoretically well motivated. We nevertheless emphasize that other cosmic inflation models lead to different SGWB frequency profiles; hence, they require separate dedicated analyses. See, e.g., the recent work [137] for a classification of possible inflationary SGWB shapes. Explicit particle physics models leading to Eq. (3.8) are based on the dynamics of the aforementioned models based spectator axion field  $\chi$ , which rolls during a fraction  $\Delta N$  of  $e$ -folds of inflation. In this epoch, the axion excites vector gauge fields, through the coupling  $\chi F\tilde{F}$ . The dynamics and energy density of the latter produces a sizeable SGWB with the log-normal profile (3.8). The SGWB peak  $f_*$  occurs at scales corresponding to modes leaving the horizon during the epoch of fastest roll of  $\chi$ . The height of the peak is sensitive to the quantity  $\dot{\chi}$ , while its width depends on  $\Delta N$ . Hence, each of the parameters characterizing the ansatz (3.8) has a clear physical interpretation in terms of quantities characterizing well-motivated underlying scenarios.

In Table IV, we collect two representative scenarios (Inf1 and 2) and the associated benchmark values for the parameters corresponding to the log-normal ansatz (3.8). We present their profiles in the right panel of Fig. 7, where we also depict in blue the corresponding log-normal sensitivity curve (to be discussed in the next section).

TABLE IV. Benchmark values for cosmological inflation scenarios described by ansatz (3.8).

	$\Omega_*$	$f_*$	$\rho$
Inf1	$3 \times 10^{-10}$	0.2	0.45
Inf2	$7 \times 10^{-13}$	0.25	1.6

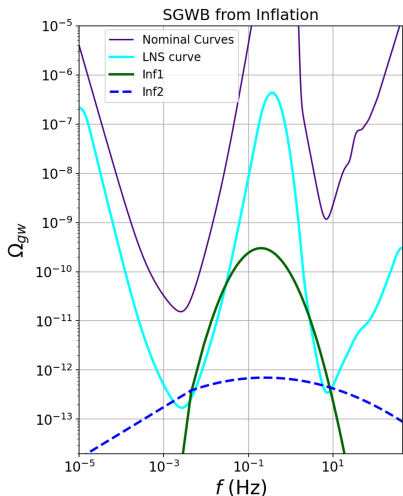


FIG. 7. Examples of SGWB from cosmic inflation; see Sec. III C. The purple curves correspond to the LISA and ET nominal curves, the turquoise curve corresponds to the integrated sensitivity curve for log-normal scenarios discussed in Sec. IV, and the blue and green lines represent the benchmark scenarios in Table IV.

The parameters are selected such that their profiles peak in the middle between the LISA and ET bands, with different amplitudes and different peak sharpness. In Fig. 8, we plot the corresponding Fisher forecasts. LISA alone would be able to measure the parameters with good accuracy in scenario Inf1. On the other hand, scenario Inf2 would benefit much from the synergy between the two experiments.

In conclusion, the synergy between LISA and the ET can help in distinguishing and characterizing early-Universe sources of SGWB. In the next two sections, we develop and expand upon this topic, considering further concepts and observables to exploit the potential of making detections with the two experiments together.

#### IV. NOTION OF INTEGRATED SENSITIVITY CURVES

Is there a simple, intuitive way to know whether a given SGWB profile can be detected by GW experiments? The answer is affirmative, thanks to the notion of a sensitivity curve. In this section, we discuss various versions of sensitivity curves for LISA, the ET, and the two experiments operating together.

The concept of a nominal sensitivity curve offers a visual tool to intuitively understand whether a certain GW source with its frequency profile can be detected by a GW experiment. If a given GW signal has a sufficiently large amplitude to cross the sensitivity curve, it will automatically be detected by the particular experiment with a signal-to-noise ratio of greater than unity. The frequency profile of the nominal sensitivity curve depends on the noise sources affecting a given experiment and on the response of the latter to a GW input. We already discussed and represented the nominal sensitivity curves in Sec. II (see Fig. 2).

By inspecting Fig. 2, we can see that the frequency regions of maximal sensitivity for LISA and the ET are different (we call them  $\mathcal{B}_{\text{LISA}}$  and  $\mathcal{B}_{\text{ET}}$ ) and span the ranges

$$\mathcal{B}_{\text{LISA}} \simeq 10^{-5} \leq f/\text{Hz} \leq 10^{-1}, \quad (4.1)$$

$$\mathcal{B}_{\text{ET}} \simeq 10^0 \leq f/\text{Hz} \leq 445. \quad (4.2)$$

At face value, the detectors do not cover well (due to poor sensitivity) the intermediate region in between say  $8 \times 10^{-2} \leq f/\text{Hz} \leq 2$ . Also, the minimal nominal sensitivity of LISA to  $\Omega_{\text{GW}}$  is around 1 order of magnitude larger than the ET. We have cut off the upper limit of the frequency range for the ET at 445 Hz because, beyond this frequency, the sensitivity of the instrument decreases beyond the previously mentioned BBN limit of  $\Omega_{\text{GW}} \leq 1.7 \times 10^{-6}$ , and therefore those frequencies are not of interest to us in this work.

However, in representing the nominal sensitivity curves as discussed above, we do not make use of the crucial fact that the SGWB signal is extended over decades of frequency ranges. If such a broad frequency profile exists, we may integrate over the entire frequency range to allow us obtain more crucial information on the signal by having more large SNR. A broad frequency profile suggests that we can integrate over the frequency range, allowing us to obtain further information on the signal by collecting more SNR [see formula (2.31)]. We already came across this feature while discussing Fisher forecasts in Sec. III. For this reason, Ref. [263] introduced the notion of power-law sensitivity curve<sup>6</sup> as a useful visual device to understand whether a given signal can be detected by a GW experiment. Following Ref. [263], we start by assuming that a given signal is described by a power-law profile,

$$\Omega_{\text{GW}} = \Omega_{\star} (f/f_{\star})^{n_T}, \quad (4.3)$$

over the frequency band we are interested in, with  $f_{\star}$  a given reference frequency. The spectral tilt  $n_T$  is not exactly known, though; we assume that it can vary over an interval between two fiducial values. For each value of the tilt, we can determine the minimal value of the signal amplitude  $\Omega_{\star}$  ensures that the corresponding SNR overcomes a certain threshold. We shall consider

$$\text{SNR} = 5, \quad T = 3 \text{ years}. \quad (4.4)$$

Then, we determine the envelope of the resulting curves associated with the various spectral tilts and draw for each

<sup>6</sup>For certain signals like phase transition which carries a peak, peaked integrated sensitivity may fare better than power-law sensitivity; see Ref. [264] for details. However, in this paper, we focus to the former case for overall comparison purposes.

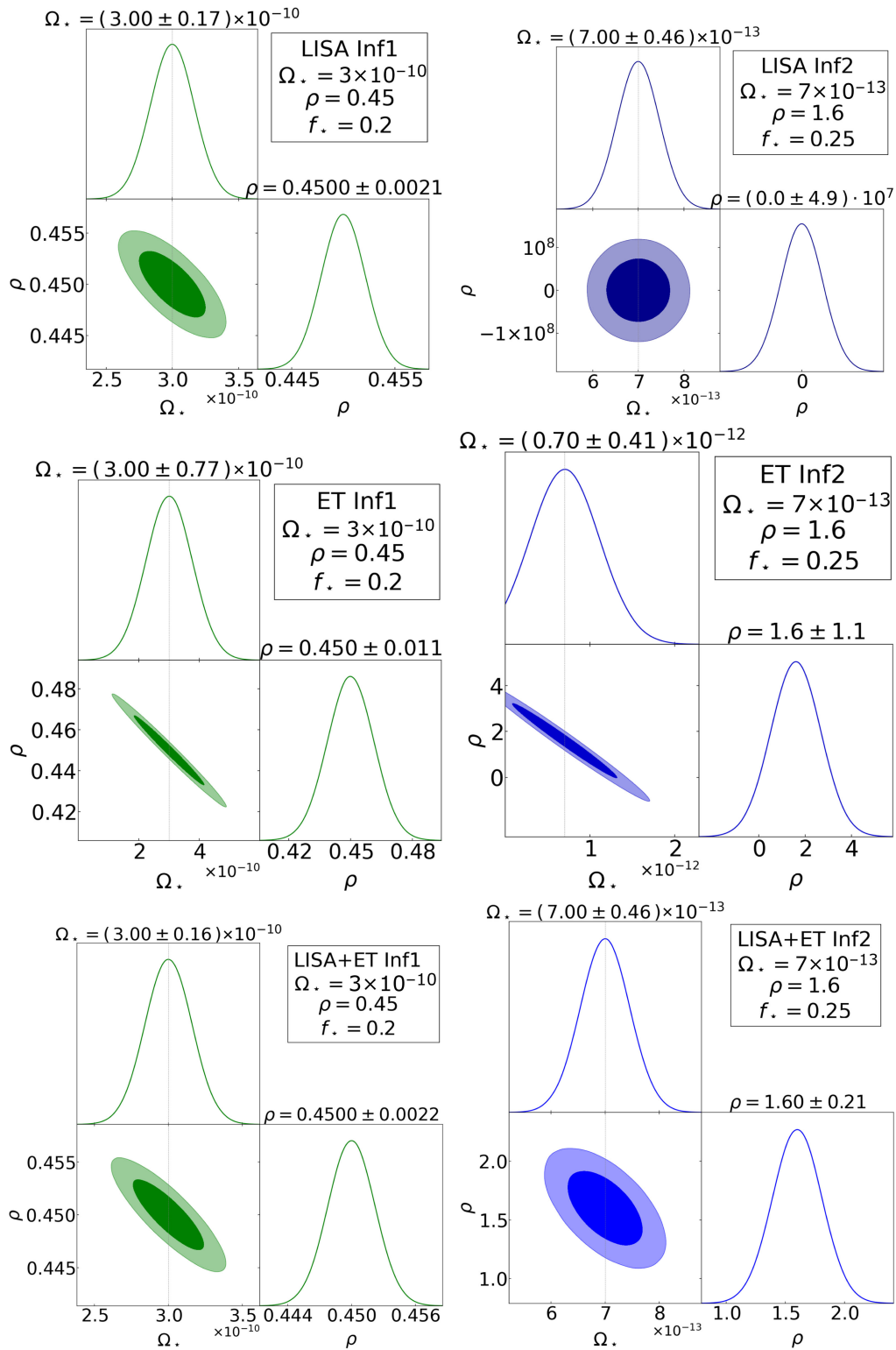


FIG. 8. Fisher forecasts for the cosmic inflation benchmark scenarios Inf1 and Inf2, as summarized in Table IV.

frequency the maximal signal amplitude after scanning over all the tilts.

The result is the so-called power-law-sensitivity curve (PLS), which we represent in Fig. 9. We allow  $n_T$  to vary

between  $-9/2 < n_T < 9/2$ , with these numbers chosen for better visualization purposes. The left and central panels show the standard PLS curves associated with LISA and the ET, built following the aforementioned algorithm.

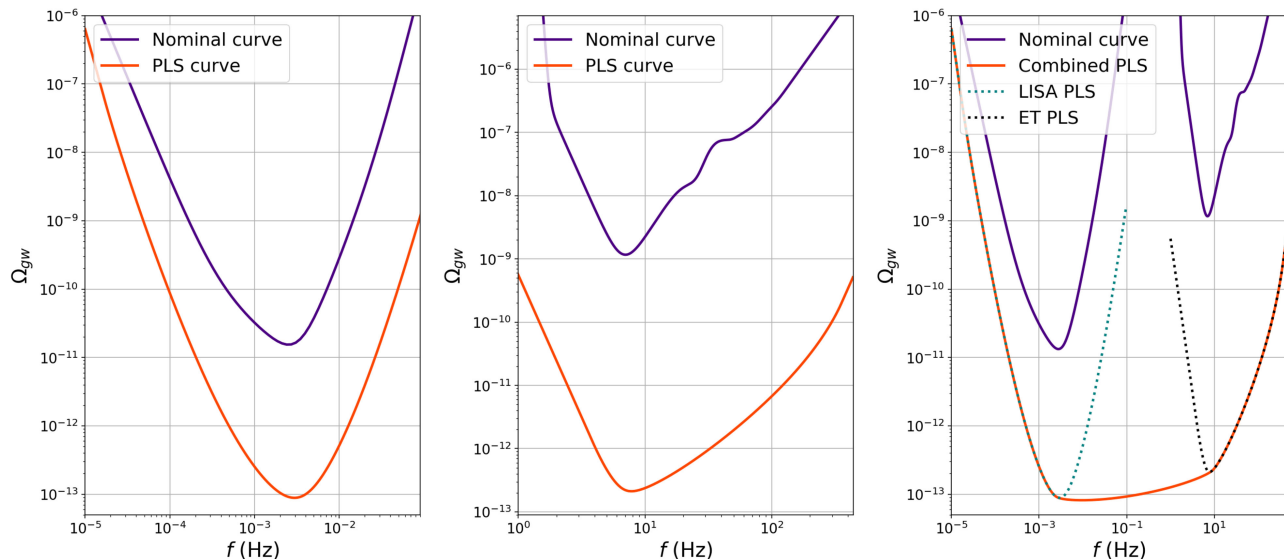


FIG. 9. Orange lines: PLS curves for LISA (left panel), the ET (central panel), and the two experiments combined (right panel). For the nominal sensitivity curves in purple, we use the analytical fits of the Appendix.

Every power-law spectrum passing above these curves can be detected by LISA (left panel) or the ET (central panel) with  $\text{SNR} > 5$ . In drawing these curves, we have assumed that the signal is a power law over the entire range of frequencies (3.1), but we measure it with one experiment only. Notice that, differently from the nominal curves, the integration over frequencies associated with the notion of PLS curves leads to a sensitivity for the ET comparable with that of LISA.

In plotting the combined PLS in the right panel of Fig. 9, we take advantage of the fact that both LISA and the ET can measure the same signal independently; hence, they can provide a multiband detection of a given SGWB. Again, we assume that the SGWB signal is a power law for the *entire* frequency range (3.1). We form the total  $\text{SNR}_{\text{tot}}$  using Eq. (2.31) and use this quantity to draw the combined PLS in the right panel of Fig. 9.

The plots in Fig. 9 demonstrate that the PLS curves gain orders of magnitude in sensitivity with respect to the nominal curves. If a power-law SGWB signal passes above the PLS (but below the nominal sensitivity curve), it can nevertheless be detected by the experiment. Notice that when LISA and the ET operate together, the PLS has a low amplitude also within the frequency interval between the sensitivity bands of the individual instruments, where the system would seem to have low sensitivity [see the comment after Eq. (4.2)]. In fact, if a power-law profile crosses in the middle of each of two experiment bands, e.g.,  $\Omega_{\text{GW}} \sim 10^{-10}$  at a frequency  $f \sim 10^{-2}$  (above the PLS of the plot of Fig. 9, right panel), it certainly crosses the sensitivity curve of one or the other experiment, as it grows toward larger or smaller frequencies through the band (3.1). This feature, due to our hypothesis that the signal is a power law in the entire band (3.1), explains the much improved PLS

sensitivity in the intermediate regions in the right panel of Fig. 9, when compared to the PLS sensitivity of the individual experiments.

### A. Broken power-law and log-normal sensitivity curves

After reviewing the concept of power-law sensitivity curves, we shall now discuss the other families of integrated sensitivity curves. As discussed in Sec. III, we are interested in SGWB profiles described by a broken power law, with the frequency dependence given by the function (3.2), or log-normal profiles associated with ansatz (3.8). For this reason, we go beyond the concept of the PLS curve [263] analyzed above, and we discuss the concept of BPLS sensitivity curve as introduced in Ref. [265]. (See also Ref. [264] for previous related arguments.) We can ask what is the sensitivity of GW experiments toward detecting a SGWB with a particular SNR detection threshold, assuming a broken power-law profile within the range (3.1).

In this case, there are several parameters we can vary: the spectral tilts  $n_{1,2}$  of the growing and decreasing part of the spectrum, the position  $f_*$  of the break, and the parameter  $\sigma$  controlling the smoothness of the transition. We independently vary over the spectral tilts  $n_{1,2}$  in the interval  $-9/2 \leq n_{1,2} \leq 9/2$ , over  $1 < \sigma < 10.2$ , as well as over the values of  $f_*$  in the ranges of sensitivity of the system. We determine the minimal amplitude in Eq. (3.2) to ensure we reach an  $\text{SNR} = 5$  for each set of values of the parameters we examine, and we draw the envelope of the corresponding curves. In the left and central panels of Fig. 10, we focus on the individual experiments LISA and the ET, varying  $f_*$ , respectively, within the  $\mathcal{B}_{\text{LISA}}$  and  $\mathcal{B}_{\text{ET}}$  bands of Eq. (4.1). On the right panel, we consider the two

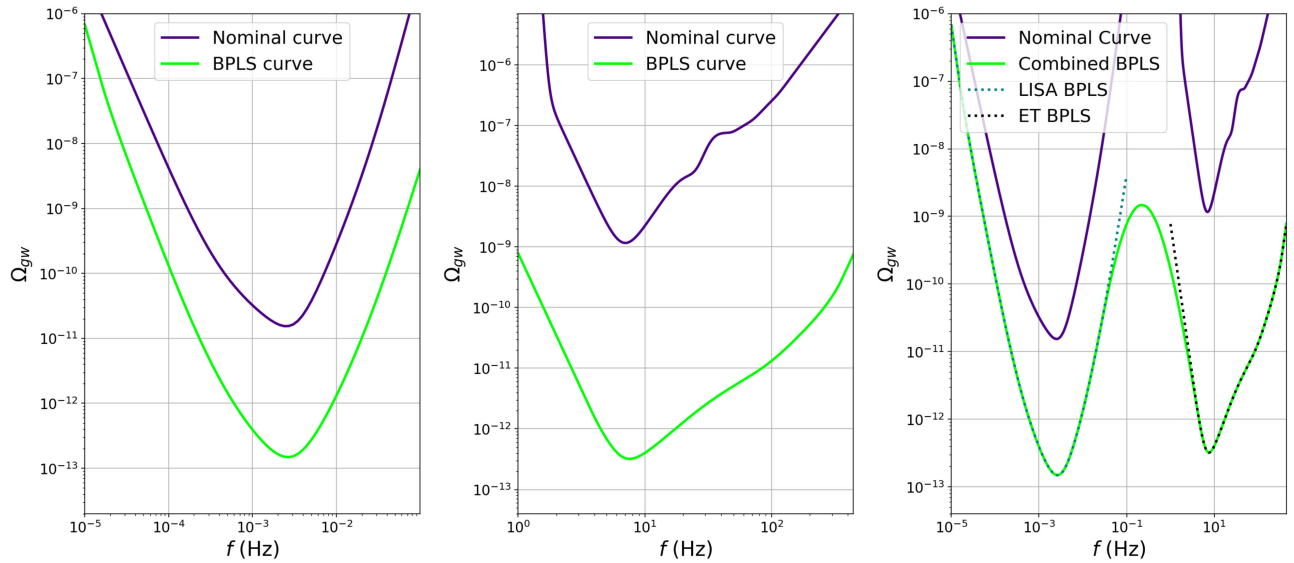


FIG. 10. Representation of the broken power-law (BPLS) sensitivity curves, as discussed in the main text.

experiments together and vary the break position  $f_*$  over the entire range (3.1).

While for the LISA-only and ET-only cases, the BPLS curves result in similar shapes and amplitude as the PLS curves in the previous subsection (compare the left and central panels of Figs. 9 and 10), the BPLS curve for the two experiments together is very different compared to the PLS curve for the two experiments (compare the right panels of Figs. 9 and 10). The reason for this difference is that the break of the BPL might occur in between the LISA and ET bands, where the sensitivity is reduced, and BPL spectra with large spectral tilts (in absolute value) might enter only partially within the sensitivity region of an experiment. Nevertheless, the plot suggests that we can accurately detect BPL SGWB profiles with a break in the

middle of LISA and ET bands and with a relatively small amplitude at the break position. This is a property that we have already explored in the previous section with a Fisher analysis of selected benchmark models for phase transition and cosmic string scenarios.

The method outlined above can also be applied to other SGWB profiles, such as the log-normal described by ansatz (3.8). In fact, we can build integrated sensitivity curves varying over the parameters characterizing Eq. (3.8). We do so in Fig. 11, varying over  $0.4 < \rho < 1$ , while  $f_*$  varies over the sensitivity bands of the experiments as described in the BPLS case. We notice that in this case the sensitivity of the combined LISA + ET system is not as good as the BPLS curves of Fig. 10 in the intermediate band between LISA and ET maximal sensitivities.

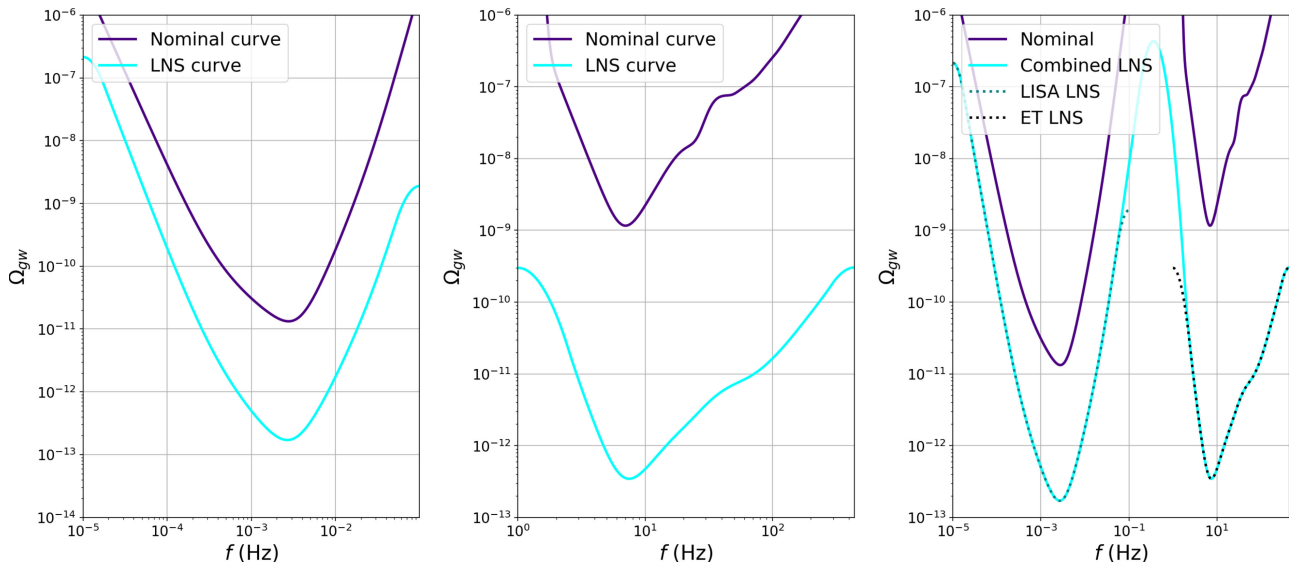


FIG. 11. Log-normal integrated sensitivity curves, built following the method discussed in the main text.

This could be because a log-normal spectrum with a sharp peak in the intermediate band may not enter the sensitivity regions of either of the two experiments at all. Nevertheless, it is important to include both profiles and carefully study the differences in their detection prospects. If we compare Fig. 3 with Fig. 7, we can see that a GW spectrum detected with a peak in the range  $10^{-9} \lesssim \Omega_{\text{GW}} \lesssim 5 \times 10^{-7}$  and  $0.1 \text{ Hz} \lesssim f \lesssim 0.9 \text{ Hz}$  is much more likely to be a broken power-law spectrum than a log-normal one. Once we know the shape of the spectrum, we can extract the parameters in the functional forms of the profiles [cf. Eqs. (3.2) and (3.8)] and use them to understand important information regarding the underlying physics, as explained in the sections delineating the two profiles. Since the different parameters correspond to different physical processes, an accurate theoretical modeling of the signal template is important for making forecasts.

As we have learned, the concept of integrated sensitivity curves offers an immediate tool to understand (or guess) the results of more sophisticated analyses based on Fisher forecasts, regarding the combined sensitivity of LISA and the ET to SGWB signals. It allows us to visually understand, in a semiquantitative manner, *why* the two experiments operating together are more powerful for detecting and characterizing a SGWB. Besides the  $\Omega_{\text{GW}}$  profile, we shall now proceed to discussing another observable which can benefit from joint GW detection: the non-Gaussianity of the SGWB.

## V. CASE OF A NON-GAUSSIAN SIGNAL

In this section, we wish to discuss at a preliminary level yet another observable which can benefit from synergies between LISA and the ET: the non-Gaussian features of the SGWB. Non-Gaussianities arise whenever nonlinearities

are important in the formation and characterization of the SGWB. It is a well-studied theme in the context of the cosmic microwave background. Yet, its physics needs to be developed further for SGWB sources.

We focus here on non-Gaussianities in the GW statistics produced during inflation (but see Ref. [266] for related studies in the context of PT). See, e.g., Ref. [267], Sec. V, for a review. It is well known that intrinsic non-Gaussianities of the SGWB are difficult to directly measure with interferometers [202,268]. In fact, Shapiro time-delay effects ruin phase correlations that are essential for characterizing most of the non-Gaussian shapes which are possible to directly detect through  $n$ -point function measurements. Exceptions are shapes corresponding to soft limits of correlation functions, such as squeezed [269,270] or collapsed limits [271] of three- or higher-point functions. In this case, momenta characterizing the Fourier modes entering correlation functions get aligned and avoid the previously mentioned dephasing time-delay effects (see Refs. [270,271] for extended discussions of aspects of the physics involved).<sup>7</sup>

Intuitively, the synergy between the LISA and ET detectors—which operate at well-separated frequency scales—represents an invaluable opportunity to probe soft limits of GW higher-point functions. Soft limits contain a large wealth of physics information (see, e.g., Ref. [276]), which would be interesting to acquire. Here, we take a small step in this direction and investigate the response of the LISA-ET system to the collapsed limit of the four-point function (the system has vanishing response to the squeezed limit of three-point function [277]). We assume that the GW four-point correlator is described by the following ansatz:

$$\begin{aligned} & \langle h^{\lambda_1}(f_1, \hat{n}_1) h^{\lambda_2}(f_2, \hat{n}_2) h^{\lambda_3}(f_3, \hat{n}_3) h^{\lambda_4}(f_4, \hat{n}_4) \rangle_{f_1 \ll f_3} \\ &= \frac{\delta^{\lambda_1 \lambda_2} \delta^{\lambda_3 \lambda_4}}{2} \delta(f_1 - f_2) \delta(f_3 - f_4) \delta^{(3)}(\hat{n}_1 + \hat{n}_2) \delta^{(3)}(\hat{n}_3 + \hat{n}_4) \delta^{(3)}(\hat{n}_1 - \hat{n}_3) S(f_1, f_3). \end{aligned} \quad (5.1)$$

The above four-point correlator in Fourier space describes a closed quadrilateral with momenta aligned and two-by-two equal in magnitude, enhanced in a soft countercollinear limit with a frequency  $f_1$  much smaller than  $f_3$ . Since  $f_{\text{LISA}} \ll f_{\text{ET}}$ , such a soft regime can be probed by our setup. We shall not discuss theoretical motivations and model building perspectives leading to the ansatz (5.1). This will be covered elsewhere, including further analysis of its consequences for GW experiments. Instead, we shall enquire how the LISA-ET system in synergy responds to the collapsed correlator described by Eq. (5.1). We wish to

measure the four-point amplitude  $S(f_1, f_3)$  in synergy between LISA and the ET. The response of the system can be obtained by a generalization of the analysis reviewed in Sec. II.

<sup>7</sup>Another possibility, which we will not further explore in this context, is to avoid correlating the GW signal directly but to instead form three- (or higher-)point functions of the SGWB *anisotropies* [272,273]. Interestingly, cross-correlations between CMB and SGWB anisotropies can also be used to test inflationary mixed tensor-scalar non-Gaussianities [274,275].

The four-point function corresponding to the measured signal—the generalization of Eq. (2.12) to higher point correlations—is

$$\begin{aligned} & \langle \Phi_{a_1 b_1 c_1}(f_1) \Phi_{a_2 b_2 c_2}(f_2) \Phi_{a_3 b_3 c_3}(f_3) \Phi_{a_4 b_4 c_4}(f_4) \rangle \\ &= \frac{\delta(f_1 - f_2) \delta(f_3 - f_4)}{2} [R^{(4)}(f_1, f_3) S(f_1, f_3) + N], \end{aligned} \quad (5.2)$$

$$\begin{aligned} R^{(4)}(f_1, f_3) = & \int \frac{d^2 \hat{n}}{4\pi} \left[ F_{a_1 b_1 c_1}^+(f_1, \hat{n}) F_{a_2 b_2 c_2}^+(-f_1, \hat{n}) + F_{a_1 b_1 c_1}^\times(f_1, \hat{n}) F_{a_2 b_2 c_2}^\times(-f_1, \hat{n}) \right]_{\text{LISA}} \\ & \times \left[ F_{a_3 b_3 c_3}^+(f_3, \hat{n}) F_{a_4 b_4 c_4}^+(-f_3, \hat{n}) + F_{a_3 b_3 c_3}^\times(f_3, \hat{n}) F_{a_4 b_4 c_4}^\times(-f_3, \hat{n}) \right]_{\text{ET}}. \end{aligned} \quad (5.3)$$

As for the case of two-point response functions, orthogonal channels can be found, and orthogonal response functions can be numerically evaluated. The complication is that the response function we are dealing with is a four-dimensional tensor. It has four indices corresponding to each interferometer channel we correlate in the soft limit—two for LISA and two for the ET. The result depends on the relative positions among all arms. As a very first step to address the subject, here we shall fix the ET arms along the directions ( $ab$ ) and ( $ac$ ) of Eq. (2.19), and we do not attempt to diagonalize the channels in the ET sector. We instead diagonalize the two remaining indices corresponding to the LISA channels.

We again call the orthogonal LISA channels  $A^\ell$ ,  $E^\ell$ , and  $T^\ell$ . The computation of such a four-point response function is similar to the diagonalization discussed in Sec. II, although the results have different amplitude and frequency dependence with respect to the two-point ones. The reason is that we have to deal with extra angular integrations when computing the integrals in Eq. (5.3). For definiteness, we fix the positions of the vertexes of the interferometer as in footnote 4. It would be interesting and

with  $R^{(4)}(f_i)$  being the four-point response function and  $N$  being the noise (to avoid cumbersome expressions, we drop indices labeling the interferometer channels). In writing the previous formula, we make use of our assumption (5.1) for the GW response function. Geometrically, the above quantity correlates measurements made at two arms of LISA and two arms of the ET, in the limit  $f_1 \ll f_3$ .  $R^{(4)}(f)$  is a generalization of the two-point response function of Eq. (2.13), formally given by the integral

important to extend our analysis to more general arm orientations.

In the small-frequency limit, the four-point response for the orthogonal channels  $A^\ell = E^\ell$  and  $T^\ell$  channels results in

$$R_{A^\ell}^{(4)} = R_{E^\ell} = \frac{27}{140} + \mathcal{O}(f/f_\star)^2, \quad (5.4)$$

$$R_{T^\ell}^{(4)} = -\frac{17}{295680} \left( \frac{f}{f_\star} \right)^4 + \mathcal{O}(f/f_\star)^6. \quad (5.5)$$

Notice that their amplitudes are different from the two-point cases of Eqs. (2.20) and (2.21), and the  $R_{T^\ell}$  now starts at small frequencies with a  $(f/f_\star)^4$  contribution, instead of a  $(f/f_\star)^6$  as in Eq. (2.21). The complete frequency dependence of the response functions can be easily obtained numerically; see Fig. 12. Suitable analytical approximations for these two quantities are given by

$$R_{A^\ell, E^\ell}^{(4)}(f) = \frac{27}{140} \left( 1 + \left( \frac{f}{1.1 f_\star} \right)^3 \right)^{-2/3}, \quad (5.6)$$

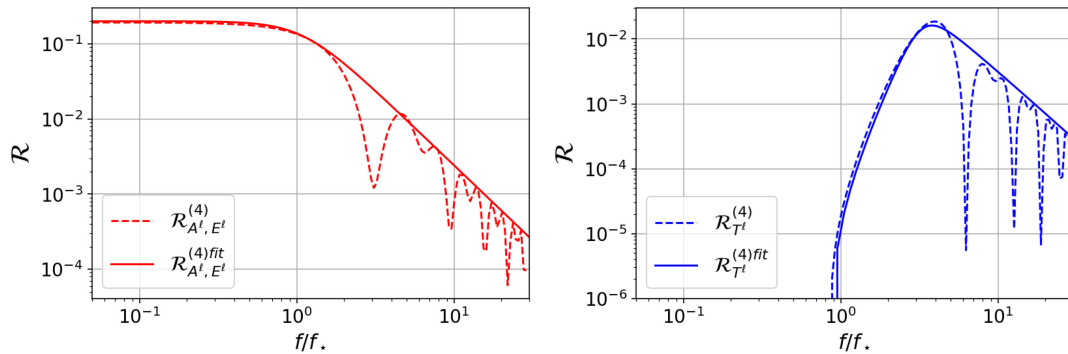


FIG. 12. The response function for the collapsed four-point function, as measurable by the LISA and the ET system, for the  $A$ ,  $E$  (left panel), and  $T$  (right panel) channels in the LISA sector. Dashed lines: numerical results. Continuous lines: the analytical approximations of Eqs. (5.6) and (5.7).

$$R_{T^c}^{(4)}(f) = \left(\frac{f}{3.3f_\star}\right)^4 \left(0.00315 \left(\frac{f}{f_\star}\right) - 0.0104\right) \times \left(1 + \left(\frac{f}{3.3f_\star}\right)^{7.2}\right)^{-1}. \quad (5.7)$$

These formulas provide the starting point for probing soft limits of GW correlation functions by considering synergies among detectors operating at different frequencies. This is a topic with several theoretical and phenomenological ramifications that we plan to develop elsewhere.

## VI. OUTLOOK

In the next decades, the GW interferometers LISA and the ET will hopefully be working around the same time. They will operate over different frequency ranges but will have similar integrated sensitivities to the amplitude of the SGWB. It is important to embark on the quest to investigate what new physics we may learn from synergies between these two detectors. We take a first small step toward that direction in this paper. Particularly, we have focused on cosmological sources of GWs, leading to a SGWB characterized by a large-amplitude and a broad-frequency spectrum spanning several decades in frequency. Operating at different frequency scales, LISA and the ET together will have the opportunity to detect distinct features of GWs produced by the same cosmological source. We quantitatively demonstrated this possibility by discussing various early-Universe examples motivated by phase transitions, cosmic strings, and inflation, showing that the synergy of the two detectors can improve our measurements of the parameters characterizing a cosmological GW source. Moreover, the two experiments operating in tandem can be sensitive to features of early-Universe cosmic expansion before big bang nucleosynthesis, which affect the SGWB frequency profile. This probe of the early Universe of the pre-BBN epoch is challenging if not impossible to test otherwise. Besides considering the GW spectrum, we additionally made a preliminary study of the sensitivity of LISA and the ET to soft limits of higher-order GW correlation functions. Given that these experiments operate over different frequency bands, their synergy constitutes an ideal direct probe of squeezed limits of non-Gaussian GW correlators and of its rich physical content.

We leave the important discussion of astrophysical SGWB and/or astrophysical noise sources to a future study. It is well known that astrophysical sources of SGWB can also lead to a broad spectrum of GWs, typically characterised by a broken power-law profile. Its shape is controlled by the type of sources of GWs (see, e.g., Ref. [278] for a review). To extract the signal and distinguish between a cosmological SGWB from the one generated by the astrophysical foregrounds, it is necessary to subtract the

astrophysical signals expected with sensitivities of Big Bang Observatory (BBO) and ET or Cosmic Explorer windows of frequency ranges [279,280]. As is well known, a binary white dwarf galactic and extragalactic astrophysical foreground also present in LISA is the dominant component as shown in Refs. [33,281,282]. This issue is quite well studied for the case of galactic white dwarfs in the LISA band (see, e.g., Ref. [283] for a recent analysis). Therefore, it should be possible to subtracted it [284–286] in order to disentangle our alluded-to cosmological effects and signal. In the entire analysis in our present work, we assume that such subtractions will be possible. If LISA and the ET operate in synergy, and if the cosmological sources lead to a sufficiently broad GW spectrum, it would be possible to obtain extra information about the signal at ET frequencies in order to “dig out” the properties of GWs in the LISA band through matched filtering techniques.

Other important simplifications we made are related to the fact that we neglected the relative motion between the two detectors, and we made simplifying assumptions about the directions of the interferometer arms. Also, we considered the noise models to be fixed, and we did not marginalize over the noise parameters. All these hypotheses will need to be extended in a more complete analysis. We leave all these interesting questions to future studies.

Ushering in the era of gravitational wave astronomy with the planned network of GW detectors worldwide aspires to and perhaps will be able to achieve measurement precisions that are orders of magnitude better with respect to the present day detectors. This new era of GW detectors, particularly with LISA and the ET, will make the dream of testing fundamental BSM microphysics, e.g., scales of new physics symmetry breaking, the scale of primordial cosmic inflation, and probing pre-BBN cosmic epochs, a reality forthcoming in a not-so-distant future.

## ACKNOWLEDGMENTS

The work of A. M. B. and G. T. is partially funded by STFC Grant No. ST/X000648/1. D. C. would like to thank the Indian Institute of Astrophysics and the Department of Science and Technology, Government of India, for support through the INSPIRE Faculty Fellowship Grant No. DST/INSPIRE/04/2023/000110. D. C. would also like to thank the Indian Institute of Science for support through the C. V. Raman postdoctoral fellowship. D. C. acknowledges the use of high-performance computational facilities at the Supercomputer Education and Research Centre (SERC) of the Indian Institute of Science and the NOVA HPC cluster at the Indian Institute of Astrophysics.

## DATA AVAILABILITY

No data were created or analyzed in this study.

## APPENDIX: ANALYTICAL FITS TO NOMINAL CURVES

For LISA, we use the analytical fits to the nominal sensitivity curve of Ref. [34], using  $h = 0.67$  (see Fig. 2, right panel). In this appendix, we report the expressions for the fit to the nominal ET-D<sup>8</sup> sensitivity curve for the Einstein Telescope, which we have presented in the left panel of Fig. 2. The fit is given by

$$\Omega_{\text{GW}}(f) = 0.88 \times (t_1 + t_2) \times t_3 t_4 t_5 t_6, \quad (\text{A1})$$

with

$$\begin{aligned} t_1 &= [9x^{-30} + 5.5 \times 10^{-6}x^{-4.5} + 28 \times 10^{-13}x^{3.2}] \times \left( \frac{1}{2} - \frac{1}{2} \tanh(0.06(x - 42)) \right), \\ t_2 &= [1 \times 10^{-13}x^{1.9} + 20 \times 10^{-13}x^{2.8}] \times \frac{1}{2} \tanh(0.06(x - 42)), \\ t_3 &= 1 - 0.475 \exp\left(-\frac{(x - 25)^2}{50}\right), \\ t_4 &= 1 - 5 \times 10^{-4} \exp\left(-\frac{(x - 20)^2}{100}\right), \\ t_5 &= 1 - 0.2 \exp\left(-\frac{((x - 47)^2)^{0.85}}{100}\right), \\ t_6 &= 1 - 0.12 \exp\left(-\frac{((x - 50)^2)^{0.7}}{100}\right) - 0.2 \exp\left(-\frac{(x - 45)^2}{250}\right) + 0.15 \exp\left(-\frac{(x - 85)^2}{400}\right), \end{aligned}$$

where  $x = f/1$  Hz.

We determined this fit by trial and error. Note that the nominal sensitivity curve provided for the Einstein Telescope, which we are fitting with the above function, is for a pair of interferometers with an opening angle of  $90^\circ$  [6]. To obtain the fit for the ET-D triangular configuration with an opening angle of  $60^\circ$ , we have to multiply the expression (A1) with a factor of  $0.816^2$ .

<sup>8</sup><http://www.et-gw.eu/index.php/etsensitivities>

- 
- [1] B. P. Abbott *et al.* (LIGO Scientific, Virgo, 1M2H, Dark Energy Camera GW-E, DES, DLT40, Las Cumbres Observatory, VINROUGE, and MASTER Collaborations), A gravitational-wave standard siren measurement of the Hubble constant, *Nature (London)* **551**, 85 (2017).
  - [2] J. Aasi *et al.* (LIGO Scientific and Virgo Collaborations), Characterization of the LIGO detectors during their sixth science run, *Classical Quantum Gravity* **32**, 115012 (2015).
  - [3] P. Amaro-Seoane *et al.* (LISA Collaboration), Laser Interferometer Space Antenna, [arXiv:1702.00786](https://arxiv.org/abs/1702.00786).
  - [4] K. Yagi and N. Seto, Detector configuration of DECIGO/BBO and identification of cosmological neutron-star binaries, *Phys. Rev. D* **83**, 044011 (2011).
  - [5] M. Punturo *et al.*, The Einstein Telescope: A third-generation gravitational wave observatory, *Classical Quantum Gravity* **27**, 194002 (2010).
  - [6] S. Hild *et al.*, Sensitivity studies for third-generation gravitational wave observatories, *Classical Quantum Gravity* **28**, 094013 (2011).
  - [7] B. P. Abbott *et al.* (LIGO Scientific Collaboration), Exploring the sensitivity of next generation gravitational wave detectors, *Classical Quantum Gravity* **34**, 044001 (2017).
  - [8] B. Allen, The Stochastic gravity wave background: Sources and detection, in *Les Houches School of Physics: Astrophysical Sources of Gravitational Radiation* (1996), pp. 373–417, [arXiv:gr-qc/9604033](https://arxiv.org/abs/gr-qc/9604033).
  - [9] C. Caprini and D. G. Figueroa, Cosmological backgrounds of gravitational waves, *Classical Quantum Gravity* **35**, 163001 (2018).
  - [10] P. Simakachorn, Charting cosmological history and new particle physics with primordial gravitational waves, Ph.D. thesis, Hamburg University (main), 2022.

- [11] G. Agazie *et al.* (NANOGrav Collaboration), The NANOGrav 15 yr data set: Evidence for a gravitational-wave background, *Astrophys. J. Lett.* **951**, L8 (2023).
- [12] D. J. Reardon *et al.*, Search for an isotropic gravitational-wave background with the Parkes pulsar timing array, *Astrophys. J. Lett.* **951**, L6 (2023).
- [13] H. Xu *et al.*, Searching for the nano-hertz stochastic gravitational wave background with the Chinese pulsar timing array data release I, *Res. Astron. Astrophys.* **23**, 075024 (2023).
- [14] J. Antoniadis *et al.* (EPTA and InPTA Collaborations), The second data release from the European pulsar timing array—III. Search for gravitational wave signals, *Astron. Astrophys.* **678**, A50 (2023).
- [15] N. Christensen, Stochastic gravitational wave backgrounds, *Rep. Prog. Phys.* **82**, 016903 (2019).
- [16] A. I. Renzini, B. Goncharov, A. C. Jenkins, and P. M. Meyers, Stochastic gravitational-wave backgrounds: Current detection efforts and future prospects, *Galaxies* **10**, 34 (2022).
- [17] P. Auclair *et al.* (LISA Cosmology Working Group), Cosmology with the laser interferometer space antenna, *Living Rev. Relativity* **26**, 5 (2023).
- [18] P. Amaro-Seoane *et al.* (LISA Collaboration), Laser Interferometer Space Antenna, [arXiv:1702.00786](https://arxiv.org/abs/1702.00786).
- [19] M. Colpi *et al.*, LISA definition study report, [arXiv:2402.07571](https://arxiv.org/abs/2402.07571).
- [20] A. Sider *et al.*, E-TEST prototype design report, [arXiv:2212.10083](https://arxiv.org/abs/2212.10083).
- [21] M. Maggiore *et al.*, Science case for the Einstein Telescope, *J. Cosmol. Astropart. Phys.* **03** (2020) 050.
- [22] A. H. Guth, The inflationary universe: A possible solution to the horizon and flatness problems, *Phys. Rev. D* **23**, 347 (1981).
- [23] A. D. Linde, A new inflationary universe scenario: A possible solution of the horizon, flatness, homogeneity, isotropy and primordial monopole problems, *Phys. Lett.* **108B**, 389 (1982).
- [24] A. Albrecht and P. J. Steinhardt, Cosmology for grand unified theories with radiatively induced symmetry breaking, *Phys. Rev. Lett.* **48**, 1220 (1982).
- [25] Y. Akrami *et al.* (Planck Collaboration), Planck 2018 results. X. Constraints on inflation, *Astron. Astrophys.* **641**, A10 (2020).
- [26] J. R. Espinosa, G. F. Giudice, E. Morgante, A. Riotto, L. Senatore, A. Strumia, and N. Tetradis, The cosmological Higgstory of the vacuum instability, *J. High Energy Phys.* **09** (2015) 174.
- [27] Y. Gouttenoire, *Beyond the Standard Model Cocktail*, Springer theses (Springer, Cham, 2022), [10.1007/978-3-031-11862-3](https://doi.org/10.1007/978-3-031-11862-3).
- [28] M. Maggiore, Gravitational wave experiments and early universe cosmology, *Phys. Rep.* **331**, 283 (2000).
- [29] T. L. Smith and R. Caldwell, LISA for cosmologists: Calculating the signal-to-noise ratio for stochastic and deterministic sources, *Phys. Rev. D* **100**, 104055 (2019).
- [30] J. D. Romano and N. J. Cornish, Detection methods for stochastic gravitational-wave backgrounds: A unified treatment, *Living Rev. Relativity* **20**, 2 (2017).
- [31] G. Mentasti and M. Peloso, ET sensitivity to the anisotropic stochastic gravitational wave background, *J. Cosmol. Astropart. Phys.* **03** (2021) 080.
- [32] M. Branchesi *et al.*, Science with the Einstein Telescope: A comparison of different designs, *J. Cosmol. Astropart. Phys.* **07** (2023) 068.
- [33] C. J. Moore, R. H. Cole, and C. P. L. Berry, Gravitational-wave sensitivity curves, *Classical Quantum Gravity* **32**, 015014 (2015).
- [34] R. Flauger, N. Karnesis, G. Nardini, M. Pieroni, A. Ricciardone, and J. Torrado, Improved reconstruction of a stochastic gravitational wave background with LISA, *J. Cosmol. Astropart. Phys.* **01** (2021) 059.
- [35] M. Tegmark, A. Taylor, and A. Heavens, Karhunen-Loeve eigenvalue problems in cosmology: How should we tackle large data sets?, *Astrophys. J.* **480**, 22 (1997).
- [36] D. Coe, Fisher matrices and confidence ellipses: A quick-start guide and software, [arXiv:0906.4123](https://arxiv.org/abs/0906.4123).
- [37] C. Caprini, D. G. Figueroa, R. Flauger, G. Nardini, M. Peloso, M. Pieroni, A. Ricciardone, and G. Tasinato, Reconstructing the spectral shape of a stochastic gravitational wave background with LISA, *J. Cosmol. Astropart. Phys.* **11** (2019) 017.
- [38] S. Kuroyanagi, T. Chiba, and T. Takahashi, Probing the universe through the stochastic gravitational wave background, *J. Cosmol. Astropart. Phys.* **11** (2018) 038.
- [39] C. Caprini, R. Jinno, M. Lewicki, E. Madge, M. Merchand, G. Nardini, M. Pieroni, A. Roper Pol, and V. Vaskonen (LISA Cosmology Working Group), Gravitational waves from first-order phase transitions in LISA: Reconstruction pipeline and physics interpretation, *J. Cosmol. Astropart. Phys.* **10** (2024) 020.
- [40] L. Pagano, L. Salvati, and A. Melchiorri, New constraints on primordial gravitational waves from Planck 2015, *Phys. Lett. B* **760**, 823 (2016).
- [41] B. P. Abbott *et al.* (LIGO Scientific and Virgo Collaborations), Search for the isotropic stochastic background using data from Advanced LIGO's second observing run, *Phys. Rev. D* **100**, 061101 (2019).
- [42] C. Caprini *et al.*, Science with the space-based interferometer eLISA. II: Gravitational waves from cosmological phase transitions, *J. Cosmol. Astropart. Phys.* **04** (2016) 001.
- [43] C. Caprini *et al.*, Detecting gravitational waves from cosmological phase transitions with LISA: An update, *J. Cosmol. Astropart. Phys.* **03** (2020) 024.
- [44] R. Jinno, B. Shakya, and J. van de Vis, Gravitational waves from feebly interacting particles in a first order phase transition, [arXiv:2211.06405](https://arxiv.org/abs/2211.06405).
- [45] A. Kosowsky, M. S. Turner, and R. Watkins, Gravitational radiation from colliding vacuum bubbles, *Phys. Rev. D* **45**, 4514 (1992).
- [46] A. Kosowsky and M. S. Turner, Gravitational radiation from colliding vacuum bubbles: Envelope approximation to many bubble collisions, *Phys. Rev. D* **47**, 4372 (1993).
- [47] M. Kamionkowski, A. Kosowsky, and M. S. Turner, Gravitational radiation from first order phase transitions, *Phys. Rev. D* **49**, 2837 (1994).

- [48] M. Hindmarsh, S. J. Huber, K. Rummukainen, and D. J. Weir, Gravitational waves from the sound of a first order phase transition, *Phys. Rev. Lett.* **112**, 041301 (2014).
- [49] M. Hindmarsh, S. J. Huber, K. Rummukainen, and D. J. Weir, Numerical simulations of acoustically generated gravitational waves at a first order phase transition, *Phys. Rev. D* **92**, 123009 (2015).
- [50] A. Kosowsky, A. Mack, and T. Kahniashvili, Gravitational radiation from cosmological turbulence, *Phys. Rev. D* **66**, 024030 (2002).
- [51] A. D. Dolgov, D. Grasso, and A. Nicolis, Relic backgrounds of gravitational waves from cosmic turbulence, *Phys. Rev. D* **66**, 103505 (2002).
- [52] C. Caprini, R. Durrer, and G. Servant, The stochastic gravitational wave background from turbulence and magnetic fields generated by a first-order phase transition, *J. Cosmol. Astropart. Phys.* **12** (2009) 024.
- [53] T. Ghosh, A. Ghoshal, H.-K. Guo, F. Hajkarim, S. F. King, K. Sinha, X. Wang, and G. White, Did we hear the sound of the Universe boiling? Analysis using the full fluid velocity profiles and NANOGrav 15-year data, *J. Cosmol. Astropart. Phys.* **05** (2024) 100.
- [54] H.-k. Guo, F. Hajkarim, K. Sinha, G. White, and Y. Xiao, A precise fitting formula for gravitational wave spectra from phase transitions, *J. Cosmol. Astropart. Phys.* **02** (2025) 056.
- [55] C. Caprini, O. Pujolàs, H. Quelquejay-Leclere, F. Rompineve, and D. A. Steer, Primordial gravitational wave backgrounds from phase transitions with next generation ground based detectors, *Classical Quantum Gravity* **42**, 045015 (2025).
- [56] P. S. B. Dev, F. Ferrer, Y. Zhang, and Y. Zhang, Gravitational waves from first-order phase transition in a simple axion-like particle model, *J. Cosmol. Astropart. Phys.* **11** (2019) 006.
- [57] L. Delle Rose, G. Panico, M. Redi, and A. Tesi, Gravitational waves from supercool axions, *J. High Energy Phys.* **04** (2020) 025.
- [58] B. Von Harling, A. Pomarol, O. Pujolàs, and F. Rompineve, Peccei-Quinn phase transition at LIGO, *J. High Energy Phys.* **04** (2020) 195.
- [59] A. Conaci, L. Delle Rose, P. S. B. Dev, and A. Ghoshal, Slaying axion-like particles via gravitational waves and primordial black holes from supercooled phase transition, *J. High Energy Phys.* **12** (2024) 196.
- [60] R. D. Peccei and H. R. Quinn,  $CP$  conservation in the presence of instantons, *Phys. Rev. Lett.* **38**, 1440 (1977).
- [61] R. D. Peccei and H. R. Quinn, Constraints imposed by  $CP$  conservation in the presence of instantons, *Phys. Rev. D* **16**, 1791 (1977).
- [62] S. Weinberg, A new light boson?, *Phys. Rev. Lett.* **40**, 223 (1978).
- [63] F. Wilczek, Problem of strong  $P$  and  $T$  invariance in the presence of instantons, *Phys. Rev. Lett.* **40**, 279 (1978).
- [64] J. Preskill, M. B. Wise, and F. Wilczek, Cosmology of the invisible axion, *Phys. Lett.* **120B**, 127 (1983).
- [65] L. F. Abbott and P. Sikivie, A cosmological bound on the invisible axion, *Phys. Lett.* **120B**, 133 (1983).
- [66] M. Dine and W. Fischler, The not so harmless axion, *Phys. Lett.* **120B**, 137 (1983).
- [67] P. Svrcek and E. Witten, Axions in string theory, *J. High Energy Phys.* **06** (2006) 051.
- [68] A. Arvanitaki, S. Dimopoulos, S. Dubovsky, N. Kaloper, and J. March-Russell, String axiverse, *Phys. Rev. D* **81**, 123530 (2010).
- [69] D. J. E. Marsh, Axion cosmology, *Phys. Rep.* **643**, 1 (2016).
- [70] A. Dasgupta, P. S. B. Dev, A. Ghoshal, and A. Mazumdar, Gravitational wave pathway to testable leptogenesis, *Phys. Rev. D* **106**, 075027 (2022).
- [71] P. Huang and K.-P. Xie, Leptogenesis triggered by a first-order phase transition, *J. High Energy Phys.* **09** (2022) 052.
- [72] E. J. Chun, T. P. Dutka, T. H. Jung, X. Nagels, and M. Vanvlasselaer, Bubble-assisted leptogenesis, *J. High Energy Phys.* **09** (2023) 164.
- [73] A. Azatov, M. Vanvlasselaer, and W. Yin, Baryogenesis via relativistic bubble walls, *J. High Energy Phys.* **10** (2021) 043.
- [74] D. Borah, A. Dasgupta, and I. Saha, Leptogenesis and dark matter through relativistic bubble walls with observable gravitational waves, *J. High Energy Phys.* **11** (2022) 136.
- [75] C. Badger *et al.*, Probing early Universe supercooled phase transitions with gravitational wave data, *Phys. Rev. D* **107**, 023511 (2023).
- [76] P. Schwaller, Gravitational waves from a dark phase transition, *Phys. Rev. Lett.* **115**, 181101 (2015).
- [77] C. Grojean and G. Servant, Gravitational waves from phase transitions at the electroweak scale and beyond, *Phys. Rev. D* **75**, 043507 (2007).
- [78] C. Caprini, R. Durrer, T. Konstandin, and G. Servant, General properties of the gravitational wave spectrum from phase transitions, *Phys. Rev. D* **79**, 083519 (2009).
- [79] M. Lewicki and V. Vaskonen, Gravitational waves from bubble collisions and fluid motion in strongly supercooled phase transitions, *Eur. Phys. J. C* **83**, 109 (2023).
- [80] A. Lewis, GetDist: A Python package for analysing Monte Carlo samples, [arXiv:1910.13970](https://arxiv.org/abs/1910.13970).
- [81] H. B. Nielsen and P. Olesen, Vortex line models for dual strings, *Nucl. Phys.* **B61**, 45 (1973).
- [82] T. W. B. Kibble, Topology of cosmic domains and strings, *J. Phys. A* **9**, 1387 (1976).
- [83] E. J. Copeland, R. C. Myers, and J. Polchinski, Cosmic F and D strings, *J. High Energy Phys.* **06** (2004) 013.
- [84] G. Dvali and A. Vilenkin, Formation and evolution of cosmic D strings, *J. Cosmol. Astropart. Phys.* **03** (2004) 010.
- [85] J. Polchinski, Introduction to cosmic F- and D-strings, in NATO Advanced Study Institute and EC Summer School on String Theory: From Gauge Interactions to Cosmology (2004), pp. 229–253, [arXiv:hep-th/0412244](https://arxiv.org/abs/hep-th/0412244).
- [86] M. G. Jackson, N. T. Jones, and J. Polchinski, Collisions of cosmic F and D-strings, *J. High Energy Phys.* **10** (2005) 013.
- [87] S. H. H. Tye, I. Wasserman, and M. Wyman, Scaling of multi-tension cosmic superstring networks, *Phys. Rev. D* **71**, 103508 (2005); **71**, 129906(E) (2005).
- [88] A. Vilenkin, Gravitational radiation from cosmic strings, *Phys. Lett.* **107B**, 47 (1981).
- [89] A. Vilenkin, Gravitational field of vacuum domain walls and strings, *Phys. Rev. D* **23**, 852 (1981).

- [90] T. Vachaspati and A. Vilenkin, Gravitational radiation from cosmic strings, *Phys. Rev. D* **31**, 3052 (1985).
- [91] M. B. Hindmarsh and T. W. B. Kibble, Cosmic strings, *Rep. Prog. Phys.* **58**, 477 (1995).
- [92] A. Vilenkin and E. P. S. Shellard, *Cosmic Strings and Other Topological Defects* (Cambridge University Press, Cambridge, England, 2000).
- [93] T. Damour and A. Vilenkin, Gravitational wave bursts from cosmic strings, *Phys. Rev. Lett.* **85**, 3761 (2000).
- [94] A. Albrecht and N. Turok, Evolution of cosmic strings, *Phys. Rev. Lett.* **54**, 1868 (1985).
- [95] D. P. Bennett and F. R. Bouchet, Evidence for a scaling solution in cosmic string evolution, *Phys. Rev. Lett.* **60**, 257 (1988).
- [96] B. Allen and E. P. S. Shellard, Cosmic string evolution: A numerical simulation, *Phys. Rev. Lett.* **64**, 119 (1990).
- [97] C. J. A. P. Martins and E. P. S. Shellard, Extending the velocity dependent one scale string evolution model, *Phys. Rev. D* **65**, 043514 (2002).
- [98] D. G. Figueroa, M. Hindmarsh, and J. Urrestilla, Exact scale-invariant background of gravitational waves from cosmic defects, *Phys. Rev. Lett.* **110**, 101302 (2013).
- [99] C. J. A. P. Martins, I. Y. Rybak, A. Avgoustidis, and E. P. S. Shellard, Extending the velocity-dependent one-scale model for domain walls, *Phys. Rev. D* **93**, 043534 (2016).
- [100] Y. Cui, M. Lewicki, D. E. Morrissey, and J. D. Wells, Cosmic archaeology with gravitational waves from cosmic strings, *Phys. Rev. D* **97**, 123505 (2018).
- [101] Y. Cui, M. Lewicki, D. E. Morrissey, and J. D. Wells, Probing the pre-BBN universe with gravitational waves from cosmic strings, *J. High Energy Phys.* **01** (2019) 081.
- [102] Y. Gouttenoire, G. Servant, and P. Simakachorn, Beyond the standard models with cosmic strings, *J. Cosmol. Astropart. Phys.* **07** (2020) 032.
- [103] Y. Gouttenoire, G. Servant, and P. Simakachorn, BSM with cosmic strings: Heavy, up to EeV mass, unstable particles, *J. Cosmol. Astropart. Phys.* **07** (2020) 016.
- [104] S. Blasi, V. Brdar, and K. Schmitz, Has NANOGrav found first evidence for cosmic strings?, *Phys. Rev. Lett.* **126**, 041305 (2021).
- [105] A. Ghoshal, Y. Gouttenoire, L. Heurtier, and P. Simakachorn, Primordial black hole archaeology with gravitational waves from cosmic strings, *J. High Energy Phys.* **08** (2023) 196.
- [106] P. Auclair *et al.*, Probing the gravitational wave background from cosmic strings with LISA, *J. Cosmol. Astropart. Phys.* **04** (2020) 034.
- [107] J. J. Blanco-Pillado, Y. Cui, S. Kuroyanagi, M. Lewicki, G. Nardini, M. Pieroni, I. Y. Rybak, L. Sousa, and J. M. Wachter (LISA Cosmology Working Group), Gravitational waves from cosmic strings in LISA: Reconstruction pipeline and physics interpretation, [arXiv:2405.03740](https://arxiv.org/abs/2405.03740).
- [108] R. Abbott *et al.* (LIGO Scientific, Virgo, and KAGRA Collaborations), Constraints on cosmic strings using data from the third Advanced LIGO–Virgo observing run, *Phys. Rev. Lett.* **126**, 241102 (2021).
- [109] W. Buchmuller, V. Domcke, and K. Schmitz, Meta-stable cosmic strings, *J. Cosmol. Astropart. Phys.* **11** (2023) 020.
- [110] C.-F. Chang and Y. Cui, Gravitational waves from global cosmic strings and cosmic archaeology, *J. High Energy Phys.* **03** (2022) 114.
- [111] L. Sousa and P. P. Avelino, Probing cosmic superstrings with gravitational waves, *Phys. Rev. D* **94**, 063529 (2016).
- [112] P. Auclair, S. Blasi, V. Brdar, and K. Schmitz, Gravitational waves from current-carrying cosmic strings, *J. Cosmol. Astropart. Phys.* **04** (2023) 009.
- [113] I. Y. Rybak and L. Sousa, Emission of gravitational waves by superconducting cosmic strings, *J. Cosmol. Astropart. Phys.* **11** (2022) 024.
- [114] D. I. Dunskey, A. Ghoshal, H. Murayama, Y. Sakakihara, and G. White, GUTs, hybrid topological defects, and gravitational waves, *Phys. Rev. D* **106**, 075030 (2022).
- [115] R. Allahverdi *et al.*, The first three seconds: A review of possible expansion histories of the early universe, *Open J. Astrophys.* (2021), [10.21105/astro.2006.16182](https://doi.org/10.21105/astro.2006.16182).
- [116] A. Vilenkin, Cosmic strings and domain walls, *Phys. Rep.* **121**, 263 (1985).
- [117] T. Hiramatsu, M. Kawasaki, and K. Saikawa, On the estimation of gravitational wave spectrum from cosmic domain walls, *J. Cosmol. Astropart. Phys.* **02** (2014) 031.
- [118] G. B. Gelmini, M. Gleiser, and E. W. Kolb, Cosmology of biased discrete symmetry breaking, *Phys. Rev. D* **39**, 1558 (1989).
- [119] D. Coulson, Z. Lalak, and B. A. Ovrut, Biased domain walls, *Phys. Rev. D* **53**, 4237 (1996).
- [120] S. E. Larsson, S. Sarkar, and P. L. White, Evading the cosmological domain wall problem, *Phys. Rev. D* **55**, 5129 (1997).
- [121] J. Preskill, S. P. Trivedi, F. Wilczek, and M. B. Wise, Cosmology and broken discrete symmetry, *Nucl. Phys.* **B363**, 207 (1991).
- [122] R. Z. Ferreira, A. Notari, O. Pujolas, and F. Rompineve, Gravitational waves from domain walls in pulsar timing array datasets, *J. Cosmol. Astropart. Phys.* **02** (2023) 001.
- [123] B. D. Fields, K. A. Olive, T.-H. Yeh, and C. Young, Big-bang nucleosynthesis after Planck, *J. Cosmol. Astropart. Phys.* **03** (2020) 010; *J. Cosmol. Astropart. Phys.* **11** (2020) E02.
- [124] N. Aghanim *et al.* (Planck Collaboration), Planck 2018 results. VI. Cosmological parameters, *Astron. Astrophys.* **641**, A6 (2020); *Astron. Astrophys.* **652**, C4(E) (2021).
- [125] N. Ramberg, W. Ratzinger, and P. Schwaller, One  $\mu$  to rule them all: CMB spectral distortions can probe domain walls, cosmic strings and low scale phase transitions, *J. Cosmol. Astropart. Phys.* **02** (2023) 039.
- [126] J. Ellis, M. Fairbairn, G. Franciolini, G. Hütsi, A. Iovino, M. Lewicki, M. Raidal, J. Urrutia, V. Vaskonen, and H. Veermäe, What is the source of the PTA GW signal?, *Phys. Rev. D* **109**, 023522 (2024).
- [127] S. Weinberg, *Cosmology* (Oxford University Press, New York, 2008).
- [128] N. Barnaby and M. Peloso, Large non-Gaussianity in axion inflation, *Phys. Rev. Lett.* **106**, 181301 (2011).
- [129] L. Sorbo, Parity violation in the cosmic microwave background from a pseudoscalar inflaton, *J. Cosmol. Astropart. Phys.* **06** (2011) 003.
- [130] S. Endlich, A. Nicolis, and J. Wang, Solid inflation, *J. Cosmol. Astropart. Phys.* **10** (2013) 011.

- [131] D. Cannone, G. Tasinato, and D. Wands, Generalised tensor fluctuations and inflation, *J. Cosmol. Astropart. Phys.* **01** (2015) 029.
- [132] N. Bartolo, D. Cannone, A. Ricciardone, and G. Tasinato, Distinctive signatures of space-time diffeomorphism breaking in EFT of inflation, *J. Cosmol. Astropart. Phys.* **03** (2016) 044.
- [133] K. N. Ananda, C. Clarkson, and D. Wands, The cosmological gravitational wave background from primordial density perturbations, *Phys. Rev. D* **75**, 123518 (2007).
- [134] D. Baumann, P. J. Steinhardt, K. Takahashi, and K. Ichiki, Gravitational wave spectrum induced by primordial scalar perturbations, *Phys. Rev. D* **76**, 084019 (2007).
- [135] G. Domènech, Scalar induced gravitational waves review, *Universe* **7**, 398 (2021).
- [136] O. Özsoy and G. Tasinato, Inflation and primordial black holes, *Universe* **9**, 203 (2023).
- [137] M. Braglia *et al.*, Gravitational waves from inflation in LISA: Reconstruction pipeline and physics interpretation, *J. Cosmol. Astropart. Phys.* **11** (2024) 032.
- [138] A. R. Liddle and D. H. Lyth, The cold dark matter density perturbation, *Phys. Rep.* **231**, 1 (1993).
- [139] R. H. Brandenberger, A. Nayeri, S. P. Patil, and C. Vafa, Tensor modes from a primordial Hagedorn phase of string cosmology, *Phys. Rev. Lett.* **98**, 231302 (2007).
- [140] M. Baldi, F. Finelli, and S. Matarrese, Inflation with violation of the null energy condition, *Phys. Rev. D* **72**, 083504 (2005).
- [141] T. Kobayashi, M. Yamaguchi, and J. Yokoyama, G-inflation: Inflation driven by the Galileon field, *Phys. Rev. Lett.* **105**, 231302 (2010).
- [142] G. Calcagni and S. Tsujikawa, Observational constraints on patch inflation in noncommutative spacetime, *Phys. Rev. D* **70**, 103514 (2004).
- [143] G. Calcagni, S. Kuroyanagi, J. Ohashi, and S. Tsujikawa, Strong Planck constraints on braneworld and non-commutative inflation, *J. Cosmol. Astropart. Phys.* **03** (2014) 052.
- [144] J. L. Cook and L. Sorbo, Particle production during inflation and gravitational waves detectable by ground-based interferometers, *Phys. Rev. D* **85**, 023534 (2012); *Phys. Rev. D* **86**, 069901(E) (2012).
- [145] S. Mukohyama, R. Namba, M. Peloso, and G. Shiu, Blue tensor spectrum from particle production during inflation, *J. Cosmol. Astropart. Phys.* **08** (2014) 036.
- [146] S. Kuroyanagi, T. Takahashi, and S. Yokoyama, Blue-tilted inflationary tensor spectrum and reheating in the light of NANOGrav results, *J. Cosmol. Astropart. Phys.* **01** (2021) 071.
- [147] P. J. E. Peebles and A. Vilenkin, Quintessential inflation, *Phys. Rev. D* **59**, 063505 (1999).
- [148] K. Dimopoulos and J. W. F. Valle, Modeling quintessential inflation, *Astropart. Phys.* **18**, 287 (2002).
- [149] Y. Akrami, R. Kallosh, A. Linde, and V. Vardanyan, Dark energy,  $\alpha$ -attractors, and large-scale structure surveys, *J. Cosmol. Astropart. Phys.* **06** (2018) 041.
- [150] D. Bettoni and J. Rubio, Quintessential inflation: A tale of emergent and broken symmetries, *Galaxies* **10**, 22 (2022).
- [151] J. Ellis, D. V. Nanopoulos, K. A. Olive, and S. Verner, Non-oscillatory no-scale inflation, *J. Cosmol. Astropart. Phys.* **03** (2021) 052.
- [152] M. Joyce and T. Prokopec, Turning around the sphaleron bound: Electroweak baryogenesis in an alternative post-inflationary cosmology, *Phys. Rev. D* **57**, 6022 (1998).
- [153] Y. Gouttenoire, G. Servant, and P. Simakachorn, Kinaton cosmology from scalar fields and gravitational-wave signatures, [arXiv:2111.01150](https://arxiv.org/abs/2111.01150).
- [154] H. Tashiro, T. Chiba, and M. Sasaki, Reheating after quintessential inflation and gravitational waves, *Classical Quantum Gravity* **21**, 1761 (2004).
- [155] N. Bernal, A. Ghoshal, F. Hajkarim, and G. Lambiase, Primordial gravitational wave signals in modified cosmologies, *J. Cosmol. Astropart. Phys.* **11** (2020) 051.
- [156] A. Ghoshal, L. Heurtier, and A. Paul, Signatures of non-thermal dark matter with kinaton and early matter domination. Gravitational waves versus laboratory searches, *J. High Energy Phys.* **12** (2022) 105.
- [157] M. Berbig and A. Ghoshal, Impact of high-scale Seesaw and Leptogenesis on inflationary tensor perturbations as detectable gravitational waves, *J. High Energy Phys.* **05** (2023) 172.
- [158] B. Barman, A. Ghoshal, B. Grzadkowski, and A. Socha, Measuring inflaton couplings via primordial gravitational waves, *J. High Energy Phys.* **07** (2023) 231.
- [159] Y.-F. Cai, C. Lin, B. Wang, and S.-F. Yan, Sound speed resonance of the stochastic gravitational wave background, *Phys. Rev. Lett.* **126**, 071303 (2021).
- [160] Y.-F. Cai, G. Domènech, A. Ganz, J. Jiang, C. Lin, and B. Wang, Parametric resonance of gravitational waves in general scalar-tensor theories, *J. Cosmol. Astropart. Phys.* **10** (2024) 027.
- [161] D. G. Figueroa and E. H. Tanin, Ability of LIGO and LISA to probe the equation of state of the early Universe, *J. Cosmol. Astropart. Phys.* **08** (2019) 011.
- [162] K. Dimopoulos, Waterfall stiff period can generate observable primordial gravitational waves, *J. Cosmol. Astropart. Phys.* **10** (2022) 027.
- [163] C. Chen, K. Dimopoulos, C. Eröncel, and A. Ghoshal, Enhanced primordial gravitational waves from a stiff post-inflationary era due to an oscillating inflaton, *Phys. Rev. D* **110**, 063554 (2024).
- [164] F. D’Eramo and K. Schmitz, Imprint of a scalar era on the primordial spectrum of gravitational waves, *Phys. Rev. Res.* **1**, 013010 (2019).
- [165] Y. Gouttenoire, G. Servant, and P. Simakachorn, Revealing the primordial irreducible inflationary gravitational-wave background with a spinning Peccei-Quinn axion, [arXiv:2108.10328](https://arxiv.org/abs/2108.10328).
- [166] J. McDonald, WIMP densities in decaying particle dominated cosmology, *Phys. Rev. D* **43**, 1063 (1991).
- [167] T. Moroi and L. Randall, Wino cold dark matter from anomaly mediated SUSY breaking, *Nucl. Phys.* **B570**, 455 (2000).
- [168] L. Visinelli and P. Gondolo, Axion cold dark matter in non-standard cosmologies, *Phys. Rev. D* **81**, 063508 (2010).
- [169] A. L. Erickcek, The dark matter annihilation boost from low-temperature reheating, *Phys. Rev. D* **92**, 103505 (2015).

- [170] A. E. Nelson and H. Xiao, Axion cosmology with early matter domination, *Phys. Rev. D* **98**, 063516 (2018).
- [171] M. Cirelli, Y. Gouttenoire, K. Petraki, and F. Sala, Homeopathic dark matter, or how diluted heavy substances produce high energy cosmic rays, *J. Cosmol. Astropart. Phys.* **02** (2019) 014.
- [172] B. Spokoiny, Deflationary universe scenario, *Phys. Lett. B* **315**, 40 (1993).
- [173] M. Joyce, Electroweak baryogenesis and the expansion rate of the universe, *Phys. Rev. D* **55**, 1875 (1997).
- [174] V. Poulin, T. L. Smith, D. Grin, T. Karwal, and M. Kamionkowski, Cosmological implications of ultralight axionlike fields, *Phys. Rev. D* **98**, 083525 (2018).
- [175] R. T. Co, D. Dunsy, N. Fernandez, A. Ghalsasi, L. J. Hall, K. Harigaya, and J. Shelton, Gravitational wave and CMB probes of axion kination, *J. High Energy Phys.* **09** (2022) 116.
- [176] L. Heurtier, A. Moursy, and L. Wacquez, Cosmological imprints of SUSY breaking in models of sgoldstinoless non-oscillatory inflation, *J. Cosmol. Astropart. Phys.* **03** (2023) 020.
- [177] A. H. Guth and E. J. Weinberg, A cosmological lower bound on the Higgs boson mass, *Phys. Rev. Lett.* **45**, 1131 (1980).
- [178] E. Witten, Cosmological consequences of a light Higgs boson, *Nucl. Phys.* **B177**, 477 (1981).
- [179] P. Creminelli, A. Nicolis, and R. Rattazzi, Holography and the electroweak phase transition, *J. High Energy Phys.* **03** (2002) 051.
- [180] L. Randall and G. Servant, Gravitational waves from warped spacetime, *J. High Energy Phys.* **05** (2007) 054.
- [181] T. Konstandin and G. Servant, Cosmological consequences of nearly conformal dynamics at the TeV scale, *J. Cosmol. Astropart. Phys.* **12** (2011) 009.
- [182] P. Baratella, A. Pomarol, and F. Rompineve, The supercooled universe, *J. High Energy Phys.* **03** (2019) 100.
- [183] A. Ghoshal and A. Salvio, Gravitational waves from fundamental axion dynamics, *J. High Energy Phys.* **12** (2020) 049.
- [184] I. Baldes, Y. Gouttenoire, and F. Sala, String fragmentation in supercooled confinement and implications for dark matter, *J. High Energy Phys.* **04** (2021) 278.
- [185] I. Baldes, Y. Gouttenoire, F. Sala, and G. Servant, Supercool composite dark matter beyond 100 TeV, *J. High Energy Phys.* **07** (2022) 084.
- [186] F. Ferrer, A. Ghoshal, and M. Lewicki, Imprints of a supercooled phase transition in the gravitational wave spectrum from a cosmic string network, *J. High Energy Phys.* **09** (2023) 036.
- [187] J. D. Barrow, E. J. Copeland, and A. R. Liddle, The evolution of black holes in an expanding Universe, *Mon. Not. R. Astron. Soc.* **253**, 675 (1991).
- [188] K. R. Dienes, L. Heurtier, F. Huang, D. Kim, T. M. P. Tait, and B. Thomas, Primordial black holes place the universe in stasis, *arXiv:2212.01369*.
- [189] K. R. Dienes, L. Heurtier, F. Huang, D. Kim, T. M. P. Tait, and B. Thomas, Stasis in an expanding universe: A recipe for stable mixed-component cosmological eras, *Phys. Rev. D* **105**, 023530 (2022).
- [190] N. Bhaumik, A. Ghoshal, and M. Lewicki, Doubly peaked induced stochastic gravitational wave background: Testing baryogenesis from primordial black holes, *J. High Energy Phys.* **07** (2022) 130.
- [191] N. Bhaumik, A. Ghoshal, R. K. Jain, and M. Lewicki, Distinct signatures of spinning PBH domination and evaporation: Doubly peaked gravitational waves, dark relics and CMB complementarity, *J. High Energy Phys.* **05** (2023) 169.
- [192] S. Matarrese, O. Pantano, and D. Saez, A general relativistic approach to the nonlinear evolution of collisionless matter, *Phys. Rev. D* **47**, 1311 (1993).
- [193] S. Matarrese, O. Pantano, and D. Saez, General relativistic dynamics of irrotational dust: Cosmological implications, *Phys. Rev. Lett.* **72**, 320 (1994).
- [194] S. Matarrese, S. Mollerach, and M. Bruni, Second order perturbations of the Einstein-de Sitter universe, *Phys. Rev. D* **58**, 043504 (1998).
- [195] C. Carbone and S. Matarrese, A unified treatment of cosmological perturbations from super-horizon to small scales, *Phys. Rev. D* **71**, 043508 (2005).
- [196] L. Alabidi, K. Kohri, M. Sasaki, and Y. Sendouda, Observable spectra of induced gravitational waves from inflation, *J. Cosmol. Astropart. Phys.* **09** (2012) 017.
- [197] L. Alabidi, K. Kohri, M. Sasaki, and Y. Sendouda, Observable induced gravitational waves from an early matter phase, *J. Cosmol. Astropart. Phys.* **05** (2013) 033.
- [198] J.-C. Hwang, D. Jeong, and H. Noh, Gauge dependence of gravitational waves generated from scalar perturbations, *Astrophys. J.* **842**, 46 (2017).
- [199] J. R. Espinosa, D. Racco, and A. Riotto, A cosmological signature of the SM Higgs instability: Gravitational waves, *J. Cosmol. Astropart. Phys.* **09** (2018) 012.
- [200] K. Kohri and T. Terada, Semianalytic calculation of gravitational wave spectrum nonlinearly induced from primordial curvature perturbations, *Phys. Rev. D* **97**, 123532 (2018).
- [201] R.-G. Cai, S. Pi, and M. Sasaki, Gravitational waves induced by non-Gaussian scalar perturbations, *Phys. Rev. Lett.* **122**, 201101 (2019).
- [202] N. Bartolo, V. De Luca, G. Franciolini, M. Peloso, D. Racco, and A. Riotto, Testing primordial black holes as dark matter with LISA, *Phys. Rev. D* **99**, 103521 (2019).
- [203] K. Inomata and T. Nakama, Gravitational waves induced by scalar perturbations as probes of the small-scale primordial spectrum, *Phys. Rev. D* **99**, 043511 (2019).
- [204] C. Yuan, Z.-C. Chen, and Q.-G. Huang, Probing primordial-black-hole dark matter with scalar induced gravitational waves, *Phys. Rev. D* **100**, 081301 (2019).
- [205] K. Inomata, K. Kohri, T. Nakama, and T. Terada, Gravitational waves induced by scalar perturbations during a gradual transition from an early matter era to the radiation era, *J. Cosmol. Astropart. Phys.* **10** (2019) 071.
- [206] K. Inomata, K. Kohri, T. Nakama, and T. Terada, Enhancement of gravitational waves induced by scalar perturbations due to a sudden transition from an early matter era to the radiation era, *Phys. Rev. D* **100**, 043532 (2019); *Phys. Rev. D* **108**, 049901(E) (2023).

- [207] Z.-C. Chen, C. Yuan, and Q.-G. Huang, Pulsar timing array constraints on primordial black holes with NANOGrav 11-year dataset, *Phys. Rev. Lett.* **124**, 251101 (2020).
- [208] C. Yuan, Z.-C. Chen, and Q.-G. Huang, Log-dependent slope of scalar induced gravitational waves in the infrared regions, *Phys. Rev. D* **101**, 043019 (2020).
- [209] V. De Luca, G. Franciolini, A. Kehagias, and A. Riotto, On the gauge invariance of cosmological gravitational waves, *J. Cosmol. Astropart. Phys.* **03** (2020) 014.
- [210] K. Tomikawa and T. Kobayashi, Gauge dependence of gravitational waves generated at second order from scalar perturbations, *Phys. Rev. D* **101**, 083529 (2020).
- [211] J.-O. Gong, Analytic integral solutions for induced gravitational waves, *Astrophys. J.* **925**, 102 (2022).
- [212] K. Inomata and T. Terada, Gauge independence of induced gravitational waves, *Phys. Rev. D* **101**, 023523 (2020).
- [213] C. Yuan, Z.-C. Chen, and Q.-G. Huang, Scalar induced gravitational waves in different gauges, *Phys. Rev. D* **101**, 063018 (2020).
- [214] G. Domènech and M. Sasaki, Hamiltonian approach to second order gauge invariant cosmological perturbations, *Phys. Rev. D* **97**, 023521 (2018).
- [215] G. Domènech, Induced gravitational waves in a general cosmological background, *Int. J. Mod. Phys. D* **29**, 2050028 (2020).
- [216] A. Ota, Induced superhorizon tensor perturbations from anisotropic non-Gaussianity, *Phys. Rev. D* **101**, 103511 (2020).
- [217] Y.-F. Cai, C. Chen, X. Tong, D.-G. Wang, and S.-F. Yan, When primordial black holes from sound speed resonance meet a stochastic background of gravitational waves, *Phys. Rev. D* **100**, 043518 (2019).
- [218] R.-G. Cai, S. Pi, S.-J. Wang, and X.-Y. Yang, Pulsar timing array constraints on the induced gravitational waves, *J. Cosmol. Astropart. Phys.* **10** (2019) 059.
- [219] R.-G. Cai, S. Pi, S.-J. Wang, and X.-Y. Yang, Resonant multiple peaks in the induced gravitational waves, *J. Cosmol. Astropart. Phys.* **05** (2019) 013.
- [220] S. Bhattacharya, S. Mohanty, and P. Parashari, Primordial black holes and gravitational waves in nonstandard cosmologies, *Phys. Rev. D* **102**, 043522 (2020).
- [221] F. Hajkarim and J. Schaffner-Bielich, Thermal history of the early universe and primordial gravitational waves from induced scalar perturbations, *Phys. Rev. D* **101**, 043522 (2020).
- [222] R.-G. Cai, S. Pi, and M. Sasaki, Universal infrared scaling of gravitational wave background spectra, *Phys. Rev. D* **102**, 083528 (2020).
- [223] G. Domènech, S. Pi, and M. Sasaki, Induced gravitational waves as a probe of thermal history of the Universe, *J. Cosmol. Astropart. Phys.* **08** (2020) 017.
- [224] X. Niu, M. H. Rahat, K. Srinivasan, and W. Xue, Gravitational wave probes of massive gauge bosons at the cosmological collider, *J. Cosmol. Astropart. Phys.* **02** (2023) 013.
- [225] X. Niu, M. H. Rahat, K. Srinivasan, and W. Xue, Parity-odd and even trispectrum from axion inflation, *J. Cosmol. Astropart. Phys.* **05** (2023) 018.
- [226] P. Adshead, J. T. Giblin, T. R. Scully, and E. I. Sfakianakis, Gauge-preheating and the end of axion inflation, *J. Cosmol. Astropart. Phys.* **12** (2015) 034.
- [227] P. Adshead, J. T. Giblin, T. R. Scully, and E. I. Sfakianakis, Magnetogenesis from axion inflation, *J. Cosmol. Astropart. Phys.* **10** (2016) 039.
- [228] P. Adshead, J. T. Giblin, and Z. J. Weiner, Gravitational waves from gauge preheating, *Phys. Rev. D* **98**, 043525 (2018).
- [229] P. Adshead, J. T. Giblin, M. Pieroni, and Z. J. Weiner, Constraining axion inflation with gravitational waves from preheating, *Phys. Rev. D* **101**, 083534 (2020).
- [230] P. Adshead, J. T. Giblin, M. Pieroni, and Z. J. Weiner, Constraining axion inflation with gravitational waves across 29 decades in frequency, *Phys. Rev. Lett.* **124**, 171301 (2020).
- [231] K. Freese, J. A. Frieman, and A. V. Olinto, Natural inflation with pseudo—Nambu-Goldstone bosons, *Phys. Rev. Lett.* **65**, 3233 (1990).
- [232] E. Silverstein and A. Westphal, Monodromy in the CMB: Gravity waves and string inflation, *Phys. Rev. D* **78**, 106003 (2008).
- [233] L. McAllister, E. Silverstein, and A. Westphal, Gravity waves and linear inflation from axion monodromy, *Phys. Rev. D* **82**, 046003 (2010).
- [234] J. E. Kim, H. P. Nilles, and M. Peloso, Completing natural inflation, *J. Cosmol. Astropart. Phys.* **01** (2005) 005.
- [235] M. Berg, E. Pajer, and S. Sjörs, Dante’s inferno, *Phys. Rev. D* **81**, 103535 (2010).
- [236] S. Dimopoulos, S. Kachru, J. McGreevy, and J. G. Wacker, N-flation, *J. Cosmol. Astropart. Phys.* **08** (2008) 003.
- [237] E. Pajer and M. Peloso, A review of axion inflation in the era of Planck, *Classical Quantum Gravity* **30**, 214002 (2013).
- [238] M. M. Anber and L. Sorbo, N-flationary magnetic fields, *J. Cosmol. Astropart. Phys.* **10** (2006) 018.
- [239] M. M. Anber and L. Sorbo, Naturally inflating on steep potentials through electromagnetic dissipation, *Phys. Rev. D* **81**, 043534 (2010).
- [240] N. Barnaby, E. Pajer, and M. Peloso, Gauge field production in axion inflation: Consequences for monodromy, non-Gaussianity in the CMB, and gravitational waves at interferometers, *Phys. Rev. D* **85**, 023525 (2012).
- [241] N. Barnaby, R. Namba, and M. Peloso, Phenomenology of a pseudo-scalar inflaton: Naturally large non-Gaussianity, *J. Cosmol. Astropart. Phys.* **04** (2011) 009.
- [242] P. D. Meerburg and E. Pajer, Observational constraints on gauge field production in axion inflation, *J. Cosmol. Astropart. Phys.* **02** (2013) 017.
- [243] M. M. Anber and L. Sorbo, Non-Gaussianities and chiral gravitational waves in natural steep inflation, *Phys. Rev. D* **85**, 123537 (2012).
- [244] A. Linde, S. Mooij, and E. Pajer, Gauge field production in supergravity inflation: Local non-Gaussianity and primordial black holes, *Phys. Rev. D* **87**, 103506 (2013).
- [245] S.-L. Cheng, W. Lee, and K.-W. Ng, Numerical study of pseudoscalar inflation with an axion-gauge field coupling, *Phys. Rev. D* **93**, 063510 (2016).

- [246] J. Garcia-Bellido, M. Peloso, and C. Unal, Gravitational waves at interferometer scales and primordial black holes in axion inflation, *J. Cosmol. Astropart. Phys.* **12** (2016) 031.
- [247] V. Domcke, M. Pieroni, and P. Binétruy, Primordial gravitational waves for universality classes of pseudoscalar inflation, *J. Cosmol. Astropart. Phys.* **06** (2016) 031.
- [248] V. Domcke, Probing inflation models with gravitational waves, in *Proceedings of the 51st Rencontres de Moriond on Cosmology* (2016), pp. 205–208, [arXiv:1605.06364](https://arxiv.org/abs/1605.06364).
- [249] M. Peloso, L. Sorbo, and C. Unal, Rolling axions during inflation: Perturbativity and signatures, *J. Cosmol. Astropart. Phys.* **09** (2016) 001.
- [250] V. Domcke and K. Mukaida, Gauge field and fermion production during axion inflation, *J. Cosmol. Astropart. Phys.* **11** (2018) 020.
- [251] J.R.C. Cuissa and D.G. Figueroa, Lattice formulation of axion inflation. Application to preheating, *J. Cosmol. Astropart. Phys.* **06** (2019) 002.
- [252] X. Niu and M.H. Rahat, NANOGrav signal from axion inflation, *Phys. Rev. D* **108**, 115023 (2023).
- [253] C.S. Machado, W. Ratzinger, P. Schwaller, and B.A. Stefanek, Audible axions, *J. High Energy Phys.* **01** (2019) 053.
- [254] C.S. Machado, W. Ratzinger, P. Schwaller, and B.A. Stefanek, Gravitational wave probes of axionlike particles, *Phys. Rev. D* **102**, 075033 (2020).
- [255] R. T. Co, K. Harigaya, and A. Pierce, Gravitational waves and dark photon dark matter from axion rotations, *J. High Energy Phys.* **12** (2021) 099.
- [256] N. Fonseca, E. Morgante, R. Sato, and G. Servant, Axion fragmentation, *J. High Energy Phys.* **04** (2020) 010.
- [257] A. Chatrchyan and J. Jaeckel, Gravitational waves from the fragmentation of axion-like particle dark matter, *J. Cosmol. Astropart. Phys.* **02** (2021) 003.
- [258] W. Ratzinger, P. Schwaller, and B.A. Stefanek, Gravitational waves from an axion-dark photon system: A lattice study, *SciPost Phys.* **11**, 001 (2021).
- [259] C. Eröncel, R. Sato, G. Servant, and P. Sørensen, ALP dark matter from kinetic fragmentation: Opening up the parameter window, *J. Cosmol. Astropart. Phys.* **10** (2022) 053.
- [260] R. Namba, M. Peloso, M. Shiraishi, L. Sorbo, and C. Unal, Scale-dependent gravitational waves from a rolling axion, *J. Cosmol. Astropart. Phys.* **01** (2016) 041.
- [261] E. Dimastrogiovanni, M. Fasiello, and T. Fujita, Primordial gravitational waves from axion-gauge fields dynamics, *J. Cosmol. Astropart. Phys.* **01** (2017) 019.
- [262] B. Thorne, T. Fujita, M. Hazumi, N. Katayama, E. Komatsu, and M. Shiraishi, Finding the chiral gravitational wave background of an axion-SU(2) inflationary model using CMB observations and laser interferometers, *Phys. Rev. D* **97**, 043506 (2018).
- [263] E. Thrane and J.D. Romano, Sensitivity curves for searches for gravitational-wave backgrounds, *Phys. Rev. D* **88**, 124032 (2013).
- [264] K. Schmitz, New sensitivity curves for gravitational-wave signals from cosmological phase transitions, *J. High Energy Phys.* **01** (2021) 097.
- [265] D. Chowdhury, G. Tasinato, and I. Zavala, The rise of the primordial tensor spectrum from an early scalar-tensor epoch, *J. Cosmol. Astropart. Phys.* **08** (2022) 010.
- [266] S. Kumar, R. Sundrum, and Y. Tsai, Non-Gaussian stochastic gravitational waves from phase transitions, *J. High Energy Phys.* **11** (2021) 107.
- [267] N. Bartolo, V. Domcke, D. G. Figueroa, J. García-Bellido, M. Peloso, M. Pieroni, A. Ricciardone, M. Sakellariadou, L. Sorbo, and G. Tasinato, Probing non-Gaussian stochastic gravitational wave backgrounds with LISA, *J. Cosmol. Astropart. Phys.* **11** (2018) 034.
- [268] A. Margalit, C.R. Contaldi, and M. Pieroni, Phase decoherence of gravitational wave backgrounds, *Phys. Rev. D* **102**, 083506 (2020).
- [269] E. Dimastrogiovanni, M. Fasiello, and G. Tasinato, Searching for fossil fields in the gravity sector, *Phys. Rev. Lett.* **124**, 061302 (2020).
- [270] C. Powell and G. Tasinato, Probing a stationary non-Gaussian background of stochastic gravitational waves with pulsar timing arrays, *J. Cosmol. Astropart. Phys.* **01** (2020) 017.
- [271] G. Tasinato, Gravitational wave non-linearities and pulsar-timing array angular correlations, *Phys. Rev. D* **105**, 083506 (2022).
- [272] N. Bartolo, D. Bertacca, S. Matarrese, M. Peloso, A. Ricciardone, A. Riotto, and G. Tasinato, Anisotropies and non-Gaussianity of the cosmological gravitational wave background, *Phys. Rev. D* **100**, 121501 (2019).
- [273] N. Bartolo, D. Bertacca, S. Matarrese, M. Peloso, A. Ricciardone, A. Riotto, and G. Tasinato, Characterizing the cosmological gravitational wave background: Anisotropies and non-Gaussianity, *Phys. Rev. D* **102**, 023527 (2020).
- [274] P. Adshead, N. Afshordi, E. Dimastrogiovanni, M. Fasiello, E.A. Lim, and G. Tasinato, Multimessenger cosmology: Correlating cosmic microwave background and stochastic gravitational wave background measurements, *Phys. Rev. D* **103**, 023532 (2021).
- [275] G. Tasinato, Non-Gaussianities and the large  $|\eta|$  approach to inflation, *Phys. Rev. D* **109**, 063510 (2024).
- [276] V. Assassi, D. Baumann, and D. Green, On soft limits of inflationary correlation functions, *J. Cosmol. Astropart. Phys.* **11** (2012) 047.
- [277] N. Seto, Non-Gaussianity analysis of GW background made by short-duration burst signals, *Phys. Rev. D* **80**, 043003 (2009).
- [278] T. Regimbau, The astrophysical gravitational wave stochastic background, *Res. Astron. Astrophys.* **11**, 369 (2011).
- [279] C. Cutler and J. Harms, BBO and the neutron-star-binary subtraction problem, *Phys. Rev. D* **73**, 042001 (2006).
- [280] T. Regimbau, M. Evans, N. Christensen, E. Katsavounidis, B. Sathyaprakash, and S. Vitale, Digging deeper: Observing primordial gravitational waves below the binary black hole produced stochastic background, *Phys. Rev. Lett.* **118**, 151105 (2017).
- [281] A. J. Farmer and E. S. Phinney, The gravitational wave background from cosmological compact binaries, *Mon. Not. R. Astron. Soc.* **346**, 1197 (2003).
- [282] P. A. Rosado, Gravitational wave background from binary systems, *Phys. Rev. D* **84**, 084004 (2011).

- [283] S. Babak, C. Caprini, D.G. Figueroa, N. Karnesis, P. Marcoccia, G. Nardini, M. Pieroni, A. Ricciardone, A. Sesana, and J. Torrado, Stochastic gravitational wave background from stellar origin binary black holes in LISA, *J. Cosmol. Astropart. Phys.* **08** (2023) 034.
- [284] D.I. Kosenko and K.A. Postnov, On the gravitational wave noise from unresolved extragalactic binaries, *Astron. Astrophys.* **336**, 786 (1998).
- [285] M.R. Adams and N.J. Cornish, Discriminating between a stochastic gravitational wave background and instrument noise, *Phys. Rev. D* **82**, 022002 (2010).
- [286] M.R. Adams and N.J. Cornish, Detecting a stochastic gravitational wave background in the presence of a galactic foreground and instrument noise, *Phys. Rev. D* **89**, 022001 (2014).